Deep-Sea Research I 105 (2015) 142–157

Contents lists available at ScienceDirect

Deep-Sea Research I

journal homepage: www.elsevier.com/locate/dsri

Formation and variability of the Lofoten basin vortex in a high-resolution ocean model

Denis L. Volkov [a,b,*], Arseny A. Kubryakov [c,d], Rick Lumpkin [b]

[a] Cooperative Institute for Marine and Atmospheric Studies, University of Miami, Miami, FL, USA
[b] Atlantic Oceanographic and Meteorological Laboratory, NOAA, Miami, FL, USA
[c] Institute of Earth Sciences, Saint Petersburg State University, Saint Petersburg, Russia
[d] Marine Hydrophysical Institute of Russian Academy of Sciences, Sevastopol, Russia

A R T I C L E I N F O

Article history:
Received 27 January 2015
Received in revised form
28 August 2015
Accepted 2 September 2015
Available online 14 September 2015

Keywords:
Lofoten Basin
Lofoten vortex
Norwegian Sea
Norwegian
Atlantic Current
Eddies
Eddy variability
Kinematic properties of eddies
Ocean modeling
MITgcm
ECCO2
Satellite altimetry
Lagrangian drifters

A B S T R A C T

The Lofoten Basin of the Norwegian Sea is characterized by a local maximum of eddy kinetic energy and it is an important transit region for the warm and saline Atlantic waters on their way towards the Arctic Ocean. Eddies are generated by the Norwegian Atlantic Current and propagate anticlockwise around the center of the basin. In situ and satellite observations have discovered a rather small (with a radius of a few tens of km), but strong quasi-permanent anticyclonic vortex that resides in the center of the Lofoten Basin near 3°E, 69.8°N. The objective of this paper is to understand how and why the vortex is formed and to investigate what processes support its stability and drive its variability. To achieve this objective, we have conducted three high-resolution numerical experiments with the mean horizontal grid spacing of 18 km, 9 km, and 4 km. The Lofoten Vortex did not form in the 18-km experiment. The most realistic (compared to available observations) simulation of the vortex is provided by the 4-km experiment, which better reproduces eddy variability in the region. The experiments thus provide experimental evidence of the importance of eddies in the formation and stability of the vortex. We demonstrate how anticyclonic eddies, that are usually stronger and more numerous in the basin than cyclonic eddies, contribute to the intensification of the Lofoten Vortex. The Lofoten Vortex itself is not stationary and drifts cyclonically within the area bounded by approximately the 3250 m isobath. The analysis of the barotropic vorticity budget in the 4-km experiment shows that the advection of the relative vorticity gradient by eddies is the main mechanism that drives the variability of the Lofoten Vortex. The direct impact of wind/buoyancy forcing is found to be small to negligible.

1. Introduction

The Lofoten Basin (LB) is situated in the northern part of the Norwegian Sea. The LB is a rather well defined topographic depression of about 3250 m depth, bounded by the Norwegian continental slope in the east, the protruding Vøring Plateau and the Helgeland Ridge in the south and southwest, and the Mohn Ridge in the northwest (Fig. 1). The Norwegian Atlantic Current (NwAC) – a direct extension of the North Atlantic Current – dominates circulation in the Norwegian Sea. The NwAC consists of a topographically controlled barotropic current along the continental slope, the Norwegian Atlantic Slope Current (NwASC), and a baroclinic jet that follows the 2000–2500 m isobaths, known as the Norwegian Atlantic Front Current (NwAFC).

The LB is the major heat reservoir in the Nordic Seas (common name for the Norwegian, Greenland, and Iceland Seas together), characterized by large ocean–atmosphere interactions (Björk et al., 2001; Nilsen and Falck, 2006; Rossby et al., 2009a). It has attracted much scientific attention because of its peculiar thermodynamical characteristics and possible importance in the global climate system. Being a transit region for the warm and saline Atlantic Water (AW), which occupies the upper 800 m (Blindheim and Rey, 2004), on its way to the Arctic Ocean, the LB is likely to play an important role in sustaining the Atlantic Meridional Overturning Circulation (e.g. Richards and Straneo, 2015). Here, the AW loses heat to the atmosphere, mixes with ambient water masses, and thus undergoes a transformation that ultimately facilitates deep-water formation. According to recent estimates (Segtnan et al., 2011), about half of the heat carried by the AW into the Norwegian Sea (250 TW) is lost due to ocean–atmosphere interactions or lateral mixing by eddies before the AW reaches the Barents Sea boundary and the Fram Strait.

Volkov et al. (2013) called the LB a “hot spot of the Nordic Seas”, because satellite altimetry observations show a local maximum of

* Correspondence to: NOAA Atlantic Oceanographic and Meteorological Laboratory, 4301 Rickenbacker Causeway, Miami, FL 33149, USA.
E-mail address: denis.volkov@noaa.gov (D.L. Volkov).

http://dx.doi.org/10.1016/j.dsr.2015.09.001
0967-0637/

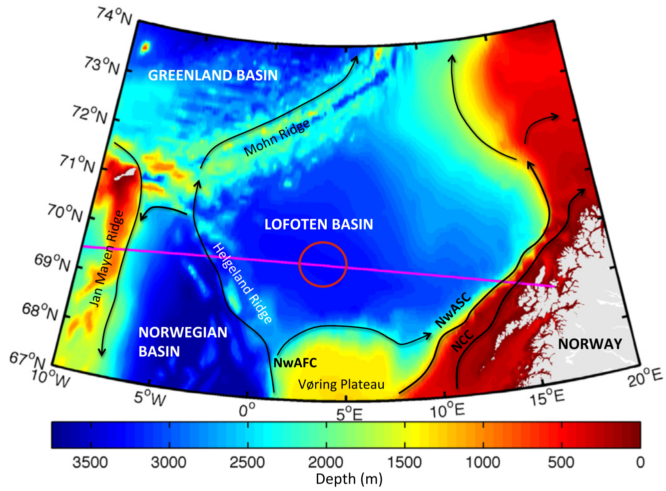

Fig. 1. Bottom topography (color) and general circulation (arrows) of the study region. The red circle marks the Lofoten Vortex location. The magenta line indicates the transect along which the vertical profiles of temperature, salinity, and velocity are analyzed. Abbreviations: NCC – Norwegian Coastal Current, NwASC – Norwegian Atlantic Slope Current, NwAFC – Norwegian Atlantic Frontal Current. (For interpretation of the references to color in this figure legend, the reader is referred to the web version of this article.)

sea surface height (SSH) variability and eddy kinetic energy (EKE). The LB eddies are found to play an important role in heat exchanges and dense water formation (Rossby et al., 2009a). Eddies are mainly generated through the instability of the NwASC (Ikeda et al., 1989; Johannessen et al., 1989; Köhl, 2007; Rossby et al. 2009b) and propagate cyclonically around the center of the LB (Volkov et al., 2013). The cyclonic propagation of SSH anomalies and the amplification of SSH variability in the center of the LB has been partly attributed to topographic Rossby waves (Volkov et al., 2013).

Russian oceanographic surveys in the 1970s and 1980s discovered a quasi-permanent anticyclonic vortex that resides in the center of the LB near 4°E and 70°N (Alexeev et al., 1991). The anticyclonic vortex (hereafter the Lofoten Vortex or simply the vortex) was characterized as a convective lens of warm and saline water in the 300–1000 m depth interval with a horizontal scale on the order of 100 km (Alexeev et al., 1991; Ivanov and Korablev, 1995a). Since that time the vortex has been observed in a number of field surveys (Rossby et al., 2009b; Andersson et al., 2011; Koszalka et al., 2011; Søiland and Rossby, 2013). Analyzing satellite altimetry maps, Raj et al. (2015) estimated the mean radius of the vortex (37 km) and the tangential speed ($\sim$30 cm s^{-1}), and found distinct seasonality in vortex's radius with winter contraction and summer expansion.

The very existence of the anticyclonic vortex in the LB is an interesting oceanic phenomenon, because the conservation of potential vorticity favors cyclonic circulations over topographic depressions in the Northern Hemisphere. Based on a sequence of oceanographic surveys and simple analytical and balance models, Ivanov and Korablev (1995b) explained the formation and stability of the vortex by winter convection, which regenerates the density anomaly and thus reinforces the associated circulation. They also suggested a seasonal cycle in the vortex's size and intensity and pointed out that the vortex can survive up to 1.5 years without external energy supply. More recently, using a numerical simulation based on the Massachusetts Institute of Technology general circulation model, Köhl (2007) argued that the vortex is formed mainly by merging of anticyclonic eddies that are shed from the NwASC. He pointed out that the topographic depression attracts the anticyclones towards its center and enables the dynamical stability of the vortex. Using satellite altimetry data, Raj et al. (2015) demonstrated a reinforcement of the Lofoten Vortex after it merged with an anticyclonic eddy. However, the spatial resolution of satellite altimetry data is too coarse to fully resolve eddy variability in the region. They also noted that buoyancy forcing might influence the long-term variability of the vortex intensity. Thus, it still remains unclear what the relative roles of buoyancy forcing and eddy merging are in generating and maintaining the Lofoten Vortex.

In this paper, we revisit the problem of the formation of the Lofoten Vortex using three numerical experiments at different eddy-permitting horizontal resolutions. By initializing the experiments with climatological fields of temperature and salinity we monitor the evolution of the eddy field in the LB and the generation of the vortex. The main focus of this study is to investigate the role of eddies in the dynamics of the vortex. Benefiting from a high-resolution model run we also estimate the kinematic properties of the Lofoten Vortex and other eddies in the LB. In addition, we investigate what processes drive the variability of the vortex strength.

2. Materials and methods

2.1. Numerical experiments

The numerical experiments are based on the Massachusetts Institute of Technology general circulation model (MITgcm; Marshall et al. 1997) nested into a global optimized solution of the Estimating the Circulation and Climate of the Ocean, Phase 2 (ECCO2, http://ecco2.jpl.nasa.gov) consortium. In essence, an ECCO2 ocean data synthesis is a least squares fit of the global full-depth-ocean and sea ice configuration of the MITgcm to selected satellite and in situ data (e.g. Menemenlis et al., 2008; Wunsch et al., 2009). The least squares fit is carried out for a small number of control parameters using a Green's function approach (Menemenlis et al., 2005). The control parameters include: initial temperature and salinity conditions; atmospheric surface boundary conditions; background vertical diffusivity; critical Richardson numbers for the Large et al. (1994) K-profile parameterization (KPP) scheme; air–ocean, ice–ocean, and air–ice drag coefficients; ice–ocean–snow albedo coefficients; bottom drag; and vertical viscosity. Data constraints include: sea level anomalies from satellite altimetry; mean dynamic topography from satellite and drifter data (Maximenko et al., 2009); satellite observations of sea surface temperature, sea ice concentration, motion, and thickness; and in situ temperature and salinity profiles (Argo, XBT, WOCE etc.). The ECCO2 optimized solution is then obtained by a free forward model integration using the adjusted control parameters. In this study, the optimized solution provides lateral boundary conditions for the numerical experiments on the nested domain.

The domain, over which the numerical experiments were carried out, was designed for multi-purpose applications and includes the North Atlantic and the Arctic Ocean (Fig. 2). The model setup is similar to the one described in Nguyen et al. (2011). The model has 50 vertical levels with intervals ranging from 10 m at the surface to 456 m at depth. Bathymetry represents a blend of the Smith and Sandwell (1997) and the General Bathymetric Charts of the Oceans (GEBCO) one-arc minute bathymetric grid. The model uses partial cell formulation of Adcroft et al. (1997), which permits accurate representation of the bathymetry. Vertical mixing follows the K-profile parameterization (KPP) of Large et al. (1994). The ocean model is coupled to the MITgcm sea ice model described in Losch et al. (2010). The model is integrated in a volume-conserving configuration using a finite volume discretization with C-grid staggering of the prognostic variables.

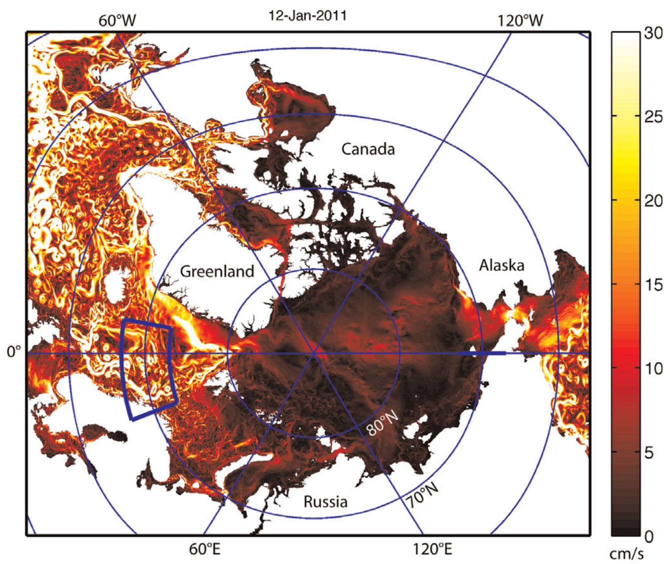

Fig. 2. Model domain: a snapshot of the absolute velocity (cm s^{-1}) at 5 m depth on January 12, 2011 from EXP04. The study region is bounded by bold blue rectangle. (For interpretation of the references to color in this figure legend, the reader is referred to the web version of this article.)

The numerical experiments were conducted at three horizontal resolutions with the mean horizontal grid spacing of $\sim$18 km, $\sim$9 km, and $\sim$4 km. According to their horizontal grid spacing, the experiments are named EXP18, EXP09, and EXP04, respectively. The 18-km grid provides the same spatial resolution as the ECCO2 ocean data synthesis. The horizontal grid of each consecutive experiment was obtained by simply dividing grid cells of the previous experiment in four cells. Thus, the horizontal grids comprise 420×384 cells in EXP18, 840×768 cells in EXP09, and 1680×1536 cells in EXP04. The experiments were initiated from climatological temperature and salinity fields, obtained from the World Ocean Atlas 2009 (WOA09) (Locarnini et al., 2010; Antonov et al., 2010). The simulations were forced with daily atmospheric state obtained from the Japanese 25-year Re-Analysis (JRA25) of the Japan Meteorological Agency (JMA). While EXP18 and EXP04 were run over 1992–2012 time interval, EXP09 was terminated in Jan 2011 after a crash. Therefore, the time-mean fields, presented in the manuscript, are computed for 1995–2010 time interval, leaving the first three years of the model spin-up out.

2.2. Observational data

To validate the numerical simulations, we use the AVISO maps of sea surface height (SSH), generated by merging multi-satellite altimetry data. The high-latitude (above 66°) data are based on either ERS-1/2 or Envisat measurements. The data are corrected for instrumental errors, geophysical effects, tidal influence, and atmospheric wind and pressure effects, and objectively interpolated to a 1/3° Mercator projection grid (Le Traon et al., 1998). Although the separation between the satellite's ground tracks and the ERS-1/2 and Envisat 35-day repeat period limits the resolution of eddy variability, the convergence of the ground tracks at high latitudes provides sufficient spatial and temporal coverage to adequately resolve the synoptic-scale variability in the Norwegian Sea (Volkov and Pujol, 2012; Volkov et al., 2013).

In addition, we use a drifter-derived seasonal climatology of global near-surface currents from Lumpkin and Johnson (2013). Drifters follow the flow integrated over the drogue depth, which is centered at 15 m. Drifter velocities are derived from finite differences of their position fixes. The velocities are archived at the Drifting Buoy Data Assembly Center of the Atlantic Oceanographic and Meteorological Laboratory (http://www.aoml.noaa.gov/phod/dac/dacdata.php), where the data are quality-controlled and interpolated to 1/4-day intervals. Specific processing has been applied to account for the slip of the drifter trajectories relative to the flow direction under direct wind forcing (Niiler and Paduan, 1995; Pazan and Niiler, 2000), and to address inhomogeneous sampling throughout the ocean, which can cause aliased time-mean values if strong seasonal and interannual variations are neglected (Lumpkin and Johnson, 2013). The drifter velocities are low-pass filtered at five days to remove high frequency variability (diurnal, tidal, inertial). The drifter-derived seasonal climatology is provided on a $1/2° \times 1/2°$ grid, but for this study we use the methodology of Lumpkin and Johnson (2013) to derive a monthly climatology on a 1/4° grid.

2.3. Determination of eddy propagation velocities

The computation of eddy propagation velocities, used as a diagnostic for the numerical experiments, is based on a space–time maximum cross-correlation method (see details in Fu, 2006, 2009). The method computes the correlations of SSH anomalies at a given location with SSH anomalies at all neighboring locations and for time lags in multiples of 7 days (the time step of the data). At each time lag, the location of the maximum correlation is identified and a velocity is estimated from the time lag and the distance of the location from the origin. An average velocity vector weighted by the correlation coefficients is ultimately computed from the estimates at various time lags. To focus on the synoptic scales, the time lags are limited to less than 12 weeks and the zonal and meridional dimensions of the box, within which the correlations between the neighboring locations are computed, are set to about 180 km. Prior to calculation, the annual, semi-annual, and interannual variability of SSH was filtered out and the spatial mean SSH was subtracted from each map to remove the residual standing oscillations.

2.4. Identification of individual eddies

In order to identify individual eddies in the model output and to obtain their kinematic properties we applied a so-called “winding angle” method. The method relies on the detection of closed streamlines in the velocity field (Sadarjoen and Post, 2000) and has already been used for the detection of oceanic eddies (e.g. Chaigneau et al., 2008). The details of the algorithm used in our study can be found in Kubryakov and Stanichny (2015). For eddy identification we used the modeled horizontal velocities at 95 m depth. The method of eddy identification consists of computing trajectories of Lagrangian particles released at all grid points on every velocity field. The total angle of deflection (winding angle) is computed for each particle at each time step of integration. The starting grid point is marked as “eddy point” if the winding angle of a particle exceeds 360°. Thus, a cluster of grid points within closed streamlines defines an eddy. The eddy radius (R) is computed from the eddy area (S): $R = \sqrt{S/\pi}$. The sense of rotation (anticyclonic/cyclonic) is determined from the eddy time-mean vorticity.

The core of the Lofoten Vortex was identified and tracked using the Okubo–Weiss (OW) parameter, $OW = s_1^2 + s_2^2 - \zeta^2$, where $s_1 = \partial v/\partial x + \partial u/\partial y$ is the shearing deformation rate, $s_2 = \partial u/\partial x - \partial v/\partial y$ is the stretching deformation rate, $\zeta = \partial v/\partial x - \partial u/\partial y$ is the relative vorticity, and u and v are the zonal and meridional velocity components, respectively (Okubo, 1970; Weiss, 1991). To objectively define the boundary of the core, we used the criterion $OW < -0.2\sigma_{OW}$, where σ_{OW} is the spatial standard deviation of OW at a particular time step. This criterion has been successfully used in previous studies for detecting eddies

(Isern-Fontanet et al., 2003, 2006; Morrow et al., 2004) as well as the Lofoten Vortex (Raj et al., 2015) from altimetry. The location of the vortex's center ($\bar{x}$, $\bar{y}$) can be obtained by averaging the (x, y) coordinates of points on the boundary. To distinguish the Lofoten Vortex from other vortices on the same map and to track the drift of the former, an identified vortex must satisfy the following constraints: the relative vorticity (ζ) must be negative (cyclones are disregarded), the radius must exceed 10 km, and the distance between the vortex's center and the location of the center at the previous time step must be the shortest.

3. Results

3.1. Horizontal circulation

The time-mean near-surface circulation obtained from satellite-tracked drifter trajectories is shown in Fig. 3. The strongest flow is associated with the NwASC and the Norwegian Coastal Current (NCC). There is a flow bifurcation on the western side of the Vøring Plateau with one branch veering eastward and eventually merging with the NwASC and the other branch flowing northwestward along the Helgeland Ridge. Very sparse drifter data in the western side of the study region, however, indicates the existence of the northeastward flow along the Mohn Ridge and the southward flow along the Jan Mayen Ridge. The most relevant to the objectives of our study observation by surface drifters is the existence of the Lofoten Vortex near 3°E and 69.8°N with orbital velocities of about 15 cm s^{-1}.

Because ocean circulation away from the coast is largely in geostrophic balance, the SSH contours represent the streamlines of the surface geostrophic flow. Fig. 4 demonstrates the SSH field averaged over the first week of the EXP18 integration. This field essentially illustrates the initial conditions (WOA09 climatological fields) of the surface flow for all numerical experiments carried out in this research. The flow is northward–northeastward all over the study region. It is rather weak over the LB and intensifies over the shelf break where the NwASC and NCC are located.

The SSH field averaged over the 1995–2010 time interval of EXP18 (Fig. 5a) does not become very much different from the initial state (Fig. 4). The streamlines still show a weak northward–northeastward flow, which feels the topography only near the Norwegian shelf. The near-surface velocities over most of the study region are approximately 5 cm and reach 20 cm in the NwASC (Fig. 5b). The Lofoten Vortex does not form, but a slight

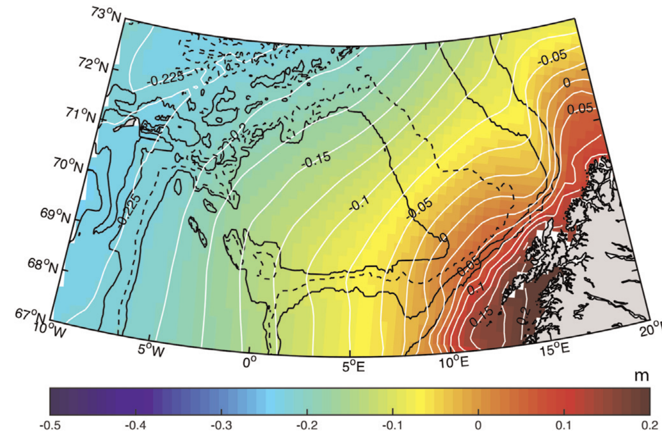

Fig. 4. Sea surface height (m) aveaged over the first week of the EXP18 simulation, similar to the initial conditions set by the WOA09 climatology. The separation between the SSH contours is 2 cm. Bottom topography (black contours) is shown for 1000, 2000, 2700 (dashed contour), and 3000 m.

anticyclonic tendency in the center of the LB develops. This is not surprising, because the horizontal resolution of EXP18 is at best 36 km, which is greater than the local Rossby radius of deformation. We estimated the Rossby radius of deformation in the LB using the methodology of Chelton et al. (1998) to vary from 20 to 25 km in both the model output and in the WOA09 (not shown).

When the resolution is doubled in EXP09 and quadrupled in EXP04, the 1995–2010 mean SSH fields (Fig. 5c and e) exhibit very different patterns compared to EXP18. The most striking feature is the formation of two SSH depressions over the Norwegian and Lofoten Basins. It should be noted that the depressions in EXP04 are stronger than in EXP09. The streamlines of the associated geostrophic flow start following the bottom topography. The near-surface (Fig. 5d and f) and depth-integrated (not shown) circulations in both basins are cyclonic, which satisfies the conservation of potential vorticity. The near-surface (15 m) velocities of the background cyclonic flow in the LB are similar for both experiments and range from 5 to 10 cm s^{-1}. Both experiments simulate a SSH rise and the associated anticyclonic vortex in the center of the LB in the position of the previously observed Lofoten Vortex. While in EXP09 the time-mean orbital velocities of the vortex are 5–7 cm s^{-1} (Fig. 5d), in EXP04 they reach about 15 cm s^{-1} (Fig. 5f). For comparison, clustering the available surface drifter data Koszalka et al. (2011) found the orbital velocities of the vortex ranging between 14 and 20 cm s^{-1} (Fig. 2d in their paper), which is closer to EXP04. It should be noted that these time-averaged velocities are smaller than possible instantaneous velocities. For example, Søiland and Rossby (2013) showed that the synoptic near-surface currents reach at least 60 cm s^{-1}. Overall, the near-surface velocities in EXP04 agree better with drifter-derived velocities from Lumpkin and Johnson (2013) (Fig. 3) than the near-surface velocities in EXP18 and EXP09.

Displayed in Fig. 6 is the evolution of the near-surface (15 m) relative vorticity averaged over the area bounded by the 2700-m isobath (shown by the dashed contour in Fig. 4) and Helgeland Ridge. One can see that in EXP18 the time-mean cyclonic circulation in the LB does not develop. The relative vorticity fluctuates around the near-zero mean with the 1995–2010 average of $\zeta_{18}=5.0\times10^{-8}$ s^{-1}. The relatively steady cyclonic flow develops in the higher resolution experiments. It is interesting to note that the spin-up time required for establishing the cyclonic circulation is about one year. The 1995–2010 mean of the relative vorticity in EXP09 is an order of magnitude greater than in EXP18 ($\zeta_9=52\times10^{-8}$ s^{-1}), while in EXP04 it is more than 2 times greater than in EXP09 ($\zeta_4=120\times10^{-8}$ s^{-1}). As seen in Fig. 6, the

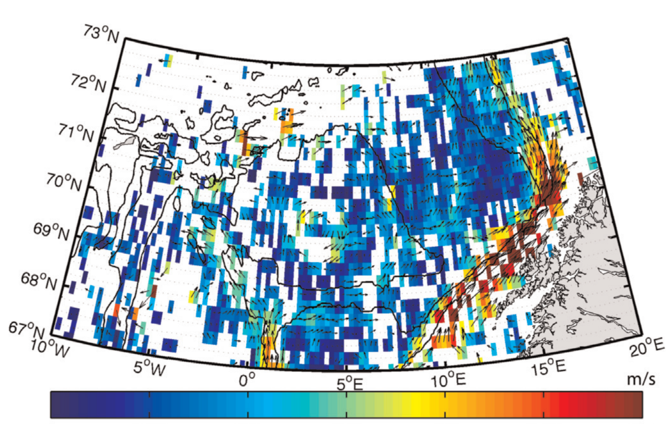

Fig. 3. The time-mean drifter-derived surface velocities (m s^{-1}) from Lumpkin and Johnson (2013). The absolute velocity is shown by the color scale. Data gaps are blanked. Bottom topography (black contours) is shown for 1000, 2000, and 3000 m. (For interpretation of the references to color in this figure legend, the reader is referred to the web version of this article.)

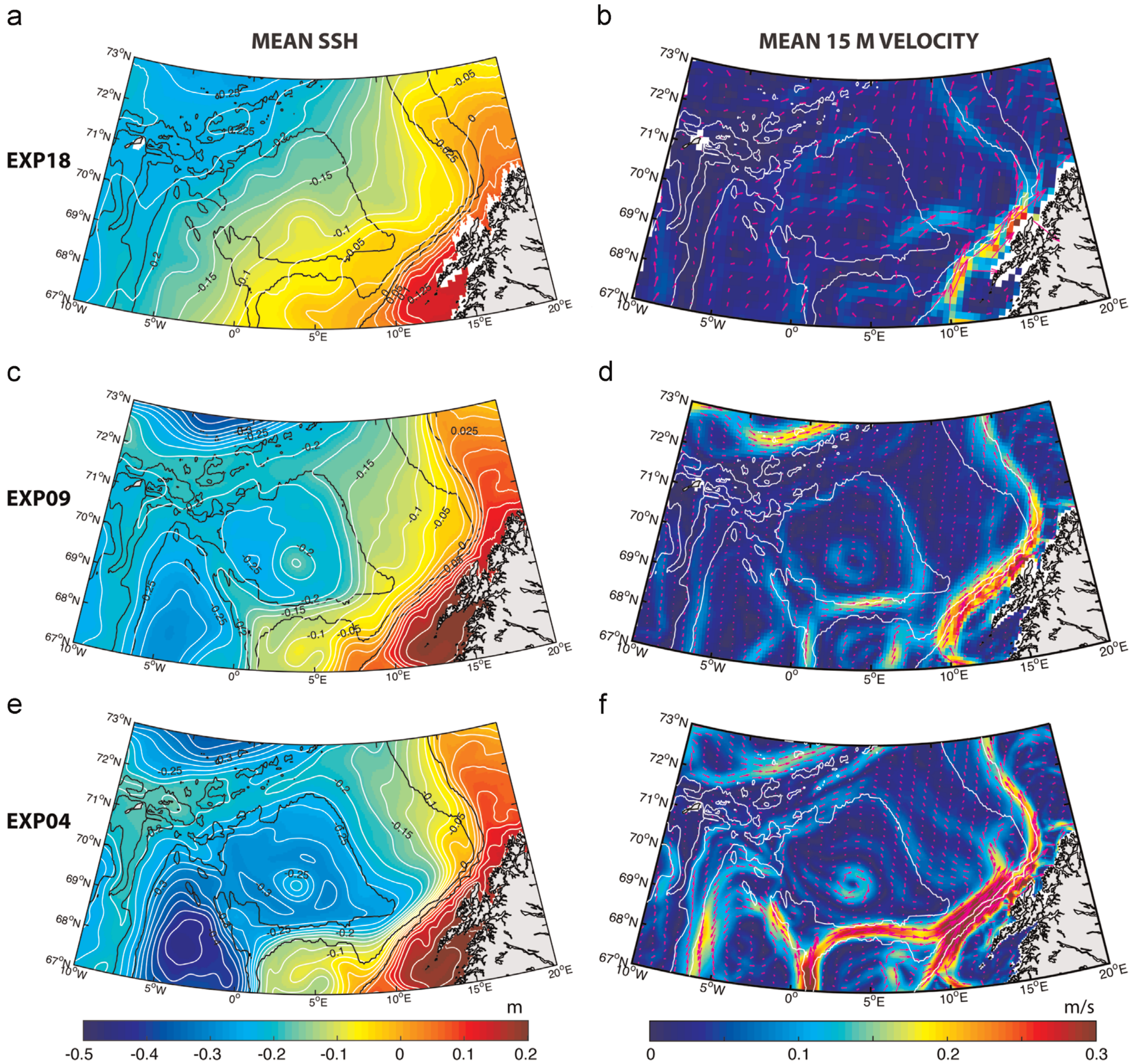

Fig. 5. Results of numerical experiments: January 1995 to December 2010 average SSH (left column) and velocity at 15 m depth (right column). The absolute velocity in the right column is shown by the color scale. Bottom topography (black contours in left column and white contours in right column) is shown for 1000, 2000, and 3000 m. (For interpretation of the references to color in this figure legend, the reader is referred to the web version of this article.)

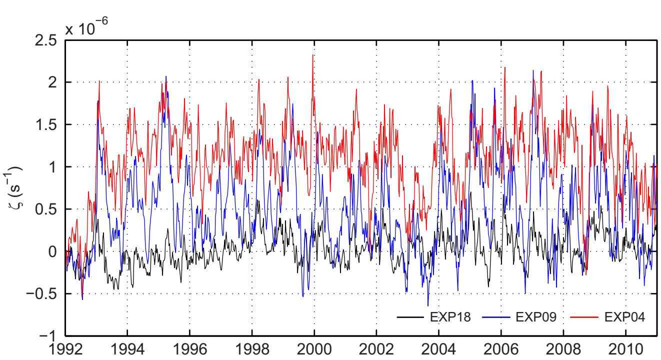

Fig. 6. Relative vorticity (s^{-1}) of circulation at 15 m depth averaged over an area with depths greater than 2700 m in the Lofoten Basin in EXP18 (black), EXP09 (blue), and EXP04 (red). The 2700-m isobath is shown in Fig. 4 by the black dashed contour. (For interpretation of the references to color in this figure legend, the reader is referred to the web version of this article.)

strength of the cyclonic circulation in the LB is subject to seasonal and interannual variability. Compared to the lower resolution runs, EXP04 features a stronger high-frequency component, which is due to an increased eddy activity in this eddy-resolving configuration of the model.

3.2. Eddy kinetic energy

Eddy activity is well characterized by eddy kinetic energy (EKE), calculated from horizontal velocity anomalies (u', v'): $EKE = 0.5(u'^2 + v'^2)$. The LB is the most eddy active region in the Nordic Seas, characterized by a local EKE maximum (Poulain et al., 1996; Volkov et al., 2013). The time-mean EKE is a good diagnostic for the model's ability to simulate mesoscale variability. Fig. 7 compares the 1995–2010 mean EKE calculated from geostrophic velocity anomalies derived from satellite altimetry (a) and model-simulated (b–d) SSH. The altimeter-derived EKE (Fig. 7a) shows a round-shaped maximum reaching 250 $cm^2\ s^{-2}$ in the center of the

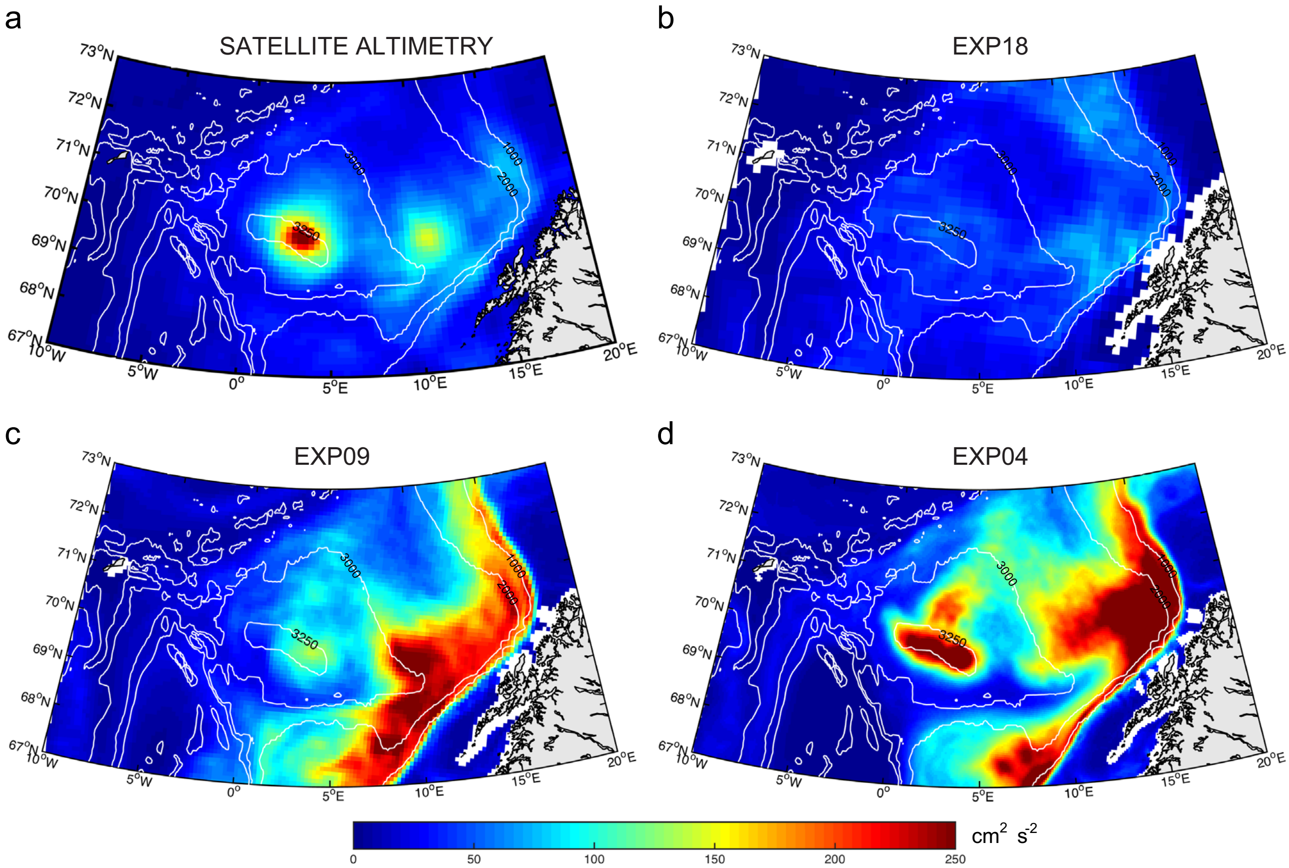

Fig. 7. Eddy kinetic energy (cm^2 s^{-2}) estimated from the satellite altimetry geostrophic velocity anomalies (a) and the model geostrophic velocity anomalies in EXP18 (b), EXP09 (c), and EXP04 (d), and averaged over the 1995–2010 time interval. Bottom topography (white contours) is shown for 1000, 2000, 3000, and 3250 m.

LB. Another local maximum of about 150 cm^2 s^{-2} is observed in the eastern part of the LB. The magnitude of EKE simulated in EXP18 (Fig. 7b) is too low compared to satellite altimetry observations. The simulated EKE is below 50 cm^2 s^{-2} in the center of the LB and it hardly reaches 100 cm^2 s^{-2} in the eastern part of the LB. The results of the EXP18 are not considered in the remaining part of the manuscript, because this experiment misrepresents the local eddy variability and it does not simulate the Lofoten Vortex.

When the horizontal resolution is doubled in EXP09, the simulated flow demonstrates much higher values of EKE (Fig. 7c). The majority of EKE is concentrated along the NwASC over the continental shelf break and just west of it. Here, the maximum EKE exceeds 250 cm^2 s^{-2}. A local EKE maximum of about 150 cm^2 s^{-2} is generated in the center of the LB, where the Lofoten Vortex resides. The magnitude of the EKE maximum in the center of the LB is more than doubled in EXP04 (Fig. 7d). It is interesting to note that the EKE maximum in EXP04 is confined within the area bounded by 3250 m isobath – the deepest part of the basin. This maximum is connected to the NwASC via a band of elevated EKE (100–150 cm^2 s^{-2}) that presumably shows the preferred path of eddy propagation from the place of origin in the NwASC to the center of the LB (e.g. Köhl, 2007; Volkov et al., 2013). These results indicate that EXP04 provides the best simulation of EKE in the center of the LB compared to satellite altimetry. The differences in the magnitude and shape of the local EKE maximum can be due to the spatial and temporal filtering of altimetry data during the objective mapping procedure and insufficient resolution. The effective spatial resolution of the present-day altimetry data products is on the order of 100 km, which exceeds the mean diameter of the Lofoten Vortex (about 80 km).

The NwASC in EXP04 also exhibits large values of EKE reaching 400 cm^2 s^{-2}. Although the strong EKE associated with the NwASC in the eastern part of the LB is not confirmed by satellite altimetry, using surface drifter trajectories Koszalka et al. (2011) presented a map of EKE that reasonably matches the one obtained from EXP04. They observed EKE reaching about 500 cm^2 s^{-2} in the eastern part of the LB and about 400 cm^2 s^{-2} in the center of the LB (Fig. 3 in Koszalka et al., 2011). Earlier, investigating the drift of RAFOS floats ballasted at about 200 m depth Rossby et al. (2009b, Fig. 12 in their paper) also estimated EKE of up to 400 cm^2 s^{-2} in the eastern part of the LB.

The reason why the altimetry-derived EKE does not show a strong maximum in the eastern part of the basin, similar to the maximum in the central part, is possibly related to the spatial and temporal resolution of altimetry data, the narrowness and orientation (~45°) of the NwASC, and the dominance of higher frequency variability. Satellite altimetry observations in the study region have mainly been provided by ERS-1 (from 1991 to 1996), ERS-2 (from 1995 to 2003), and Envisat (from 2002 to 2012) satellites that have all flown along the same 35-day repeat cycle orbit. This means that signals at one particular location along a satellite track with periods shorter than 70 days are not resolved. Due to the convergence of ground tracks at high latitudes satellite measurements are capable of capturing mesoscale variability (e.g. Volkov and Pujol, 2012), but some high-frequency intra-monthly signals are inevitably lost due to sampling issues and filtering applied during data processing. To investigate what impact the high-frequency signals in the region have on EKE estimates, we low-pass filtered the model velocities with a 1-month running mean. The EKE estimates from the low-pass filtered velocities show a much stronger reduction in the eastern part of the LB than in the central part (not shown). While EKE estimates still exceed

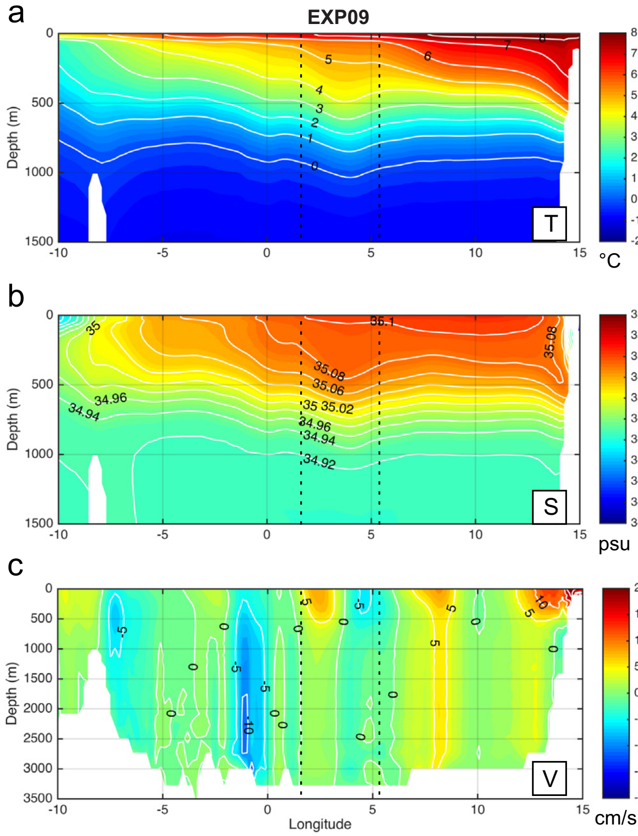

Fig. 8. Vertical profiles from EXP09 averaged over the 1995–2010 time interval: potential temperature (a), salinity (b), and velocity (c) across the transect shown in Fig. 1. The positive velocity in (c) is directed into the paper. The velocity structure associated with the time-mean position of the Lofoten Vortex is bounded by the dashed lines.

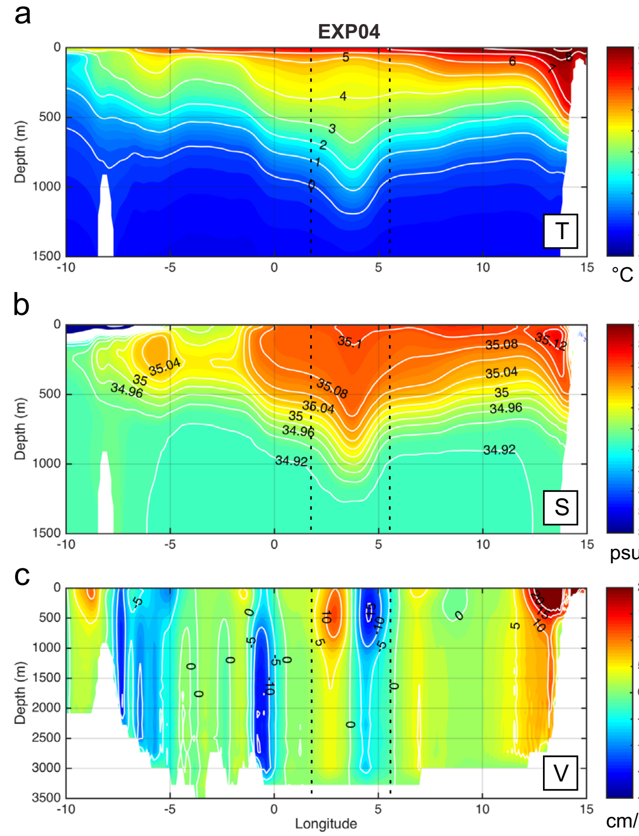

Fig. 9. Same as Fig. 8, but for EXP04.

250 $cm^2\,s^{-2}$ in the center of the LB, which is comparable to altimetry (Fig. 7a), they reach only 170 $cm^2\,s^{-2}$ in the eastern part of the LB. The area of elevated EKE near the NwASC shrinks towards the continental slope. This means that high-frequency sub-monthly signals dominate the variability in the eastern part of the LB, and present satellite altimetry measurements are not able to fully resolve them.

3.3. Vertical structure

Displayed in Figs. 8 and 9 are the vertical profiles of potential temperature, salinity, and velocity across the trans-basin transect (shown by the magenta line in Fig. 1) for EXP09 and EXP04 respectively. Both experiments exhibit a large warm pool extending from the coast of Norway in the east to Helgeland Ridge in the west. This pool is filled with the Atlantic Water that is characterized by higher salinity. Because the Lofoten Vortex is not stationary, the time–mean temperature and salinity gradients and cross-sectional velocities associated with the vortex in the Eulerian frame are smaller than in the Lagrangian frame. Therefore, in Figs. 8 and 9 we can only discuss signatures of the Lofoten Vortex.

Similar to observations (e.g. Ivanov and Korablev, 1995a; Rossby et al., 2009a,b; Raj et al., 2015), a signature of the vortex is reflected in the doming of isotherms and isohalines. This doming is considerably stronger in EXP04 (Fig. 9a and b) than in EXP09 (Fig. 8a and b). For example, the 1 °C-isotherm in EXP04 deepens to a depth of about 1000 m, which is nearly 200 m deeper than in EXP09. The experiments thus indicate an important role of the vortex in the deep mixing and penetration of the AW.

In EXP09, the time-mean cross-sectional velocities of the Lofoten Vortex in the Eulerian frame reach about 5 $cm\,s^{-1}$ and manifest maximum values near the surface (Fig. 8c). The vortex appears to be slightly barotropic with characteristic speeds of a few centimeters per second at depth. In EXP04, the signature of the vortex strengthens over the entire water column (Fig. 9c). It also shrinks near the surface and intensifies at intermediate depths. The maximum velocities of above 10 $cm\,s^{-1}$ are centered at about 500 m. For comparison, analyzing a number of hydrographic surveys, Ivanov and Korablev (1995a,b) found the core of the vortex located at depth of about 350 m with maximum velocities exceeding 6 $cm\,s^{-1}$, while Raj et al. (2015) reported on the maximum climatological velocities of 5 $cm\,s^{-1}$ at around 400 m depth.

The largely barotropic structure of circulation seen in Figs. 8c and 9c is a common feature for high-latitude flows, where the ocean is weakly stratified and geophysical flows tend to be vertically coherent (or barotropic) due to the Earth's rotation (e.g. the Antarctic Circumpolar Current). The NwASC is the strongest barotropic flow in the study region with speeds exceeding 20 $cm\,s^{-1}$ in both EXP09 and EXP04. The barotropic flows in EXP04 are stronger than in EXP09.

3.4. Eddy propagation

Because the thermohaline structure and eddy variability in the LB and the Lofoten Vortex are better represented in the 4-km simulation, from now on we use only the output of EXP04. The snapshots of 95-m depth velocities from EXP04 (Fig. 10) demonstrate examples of eddy generation by the NwASC and their subsequent propagation along a cyclonic trajectory towards the center of the LB. Eddies are formed in the eastern part of the LB (the region bounded by the magenta rectangle in Fig. 10a) due to the

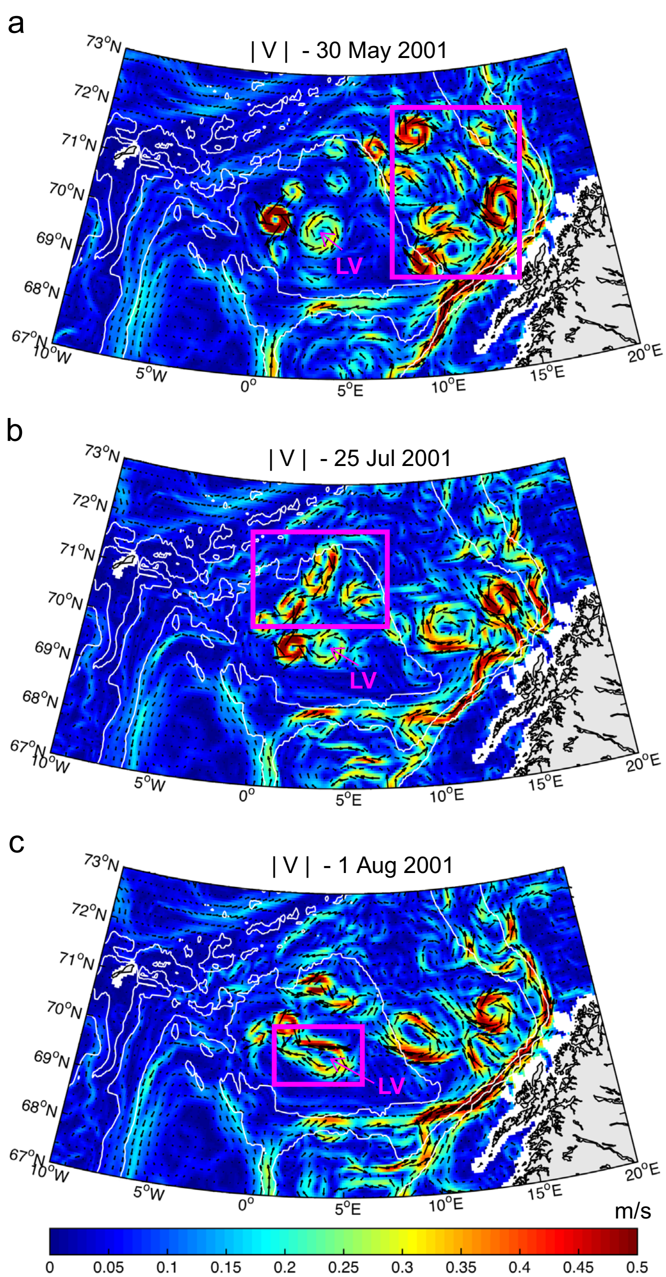

Fig. 10. Snapshots of absolute velocity at 95 m depth on (a) May 30, 2001, (b) July 25, 2001, and (c) Aug 1, 2001. Color shows the absolute velocity and arrows show the velocity vectors. Bottom topography (white contours) is shown for 1000, 2000, and 3000 m. The magenta rectangles highlight (a) the eddy generation by the NwAC, (b) multiple eddy merging events, and (c) the merging of the Lofoten Vortex (LV) with an anticyclonic eddy. (For interpretation of the references to color in this figure legend, the reader is referred to the web version of this article.)

instability of the NwASC and propagate westward. One can see that the largest and the strongest eddies with orbital speeds up to 0.5 m s^{-1} are anticyclonic and they are able to reach the western part of the LB. While eddies propagate, multiple eddy merging events may occur, which is clearly seen on July 25, 2001 (Fig. 10b, within the magenta rectangle). On the same date a strong anticyclonic eddy with orbital speeds exceeding 0.5 m s^{-1} is located just to the west of the Lofoten Vortex. The merging of this eddy with the vortex occurred around August 1, 2001 (Fig. 10c). Typically, the Lofoten Vortex is one of the strongest (if not the strongest) eddies observed in the LB. However, in the first two snapshots (Fig. 10a and b) the Lofoten Vortex is seen as a relatively weak eddy, compared to other surrounding eddies generated by

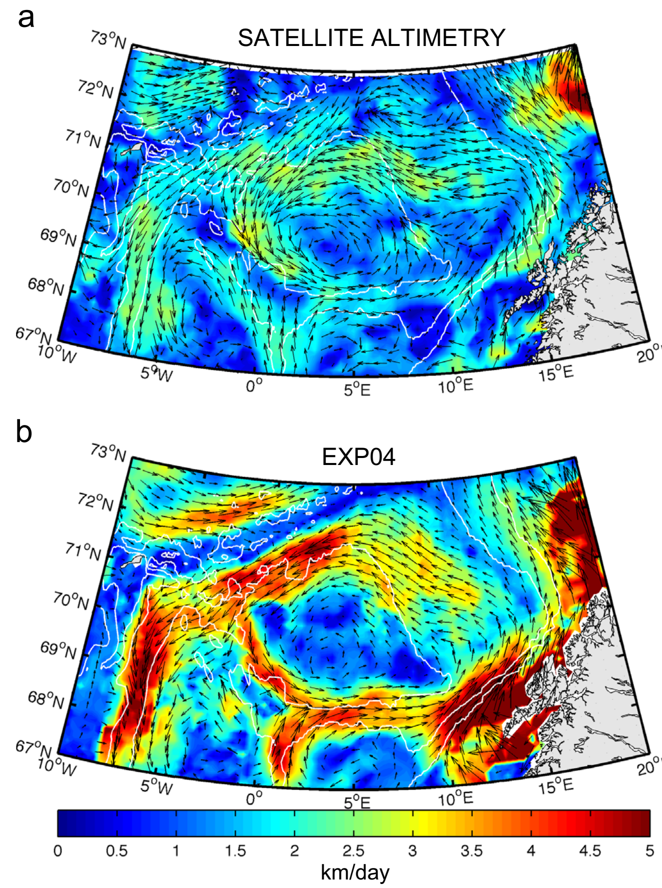

Fig. 11. Velocity of eddy propagation (km/day) derived from sea surface height anomalies measured by satellite altimetry (a) and simulated in EXP04. Bottom topography (white contours) is shown for 1000, 2000, and 3000 m.

the NwASC. This particular situation illustrates the period when the Lofoten Vortex has lost its strength, but started to accelerate during the merging process (Fig. 10c).

The cyclonic propagation of eddies in the LB was first observed with satellite altimetry (Volkov et al., 2013). Köhl (2007) suggested that eddies propagating towards the center of the LB are the main mechanism that maintains the Lofoten Vortex. The eddy propagation velocities computed from the satellite altimetry SSH using a space–time maximum cross-correlation method (described in Section 2.4) exhibit a pattern controlled by bottom topography (Fig. 11a), similar to the time-mean ocean circulation in the region. Eddies propagate along the NwAFC nearly following the 2000 m isobaths and enter the LB moving around the Vøring Plateau. Between 70°N and 71.5°N, eddies veer westward and spiral cyclonically around the center of the LB. Upon reaching the Mohn Ridge, some eddies move southwestward and then propagate southward along the Jan Mayen Ridge. The average propagation velocities in the LB are 1–3 km day^{-1}. No cyclonic eddy propagation is simulated in EXP18 (not shown). In the higher resolution experiments the eddy propagation patterns resemble those obtained from satellite altimetry. The difference between altimetry and the experiments is in the magnitude of propagation velocities. In EXP04 eddies propagate around the center of the LB with velocities 2–5 km day^{-1} (Fig. 11b).

3.5. Kinematic properties of eddies in the Lofoten basin

Benefiting from the high resolution of EXP04, it is instructive to gain knowledge on the basic kinematic properties of eddies in the LB. Here, we present such properties as the probability of the

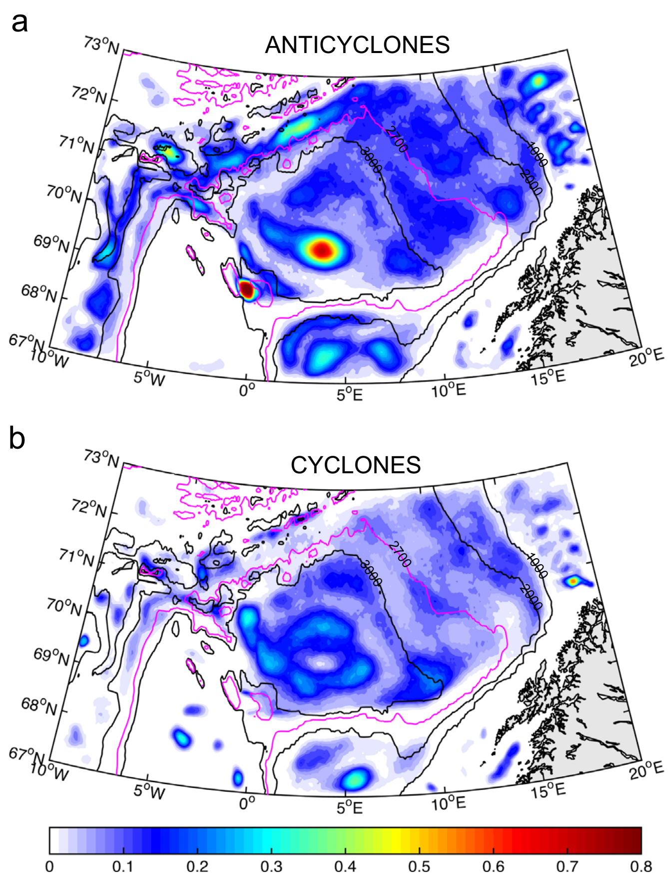

Fig. 12. The probability of (a) anticyclones and (b) cyclones, estimated from the velocity at 95 m depth and expressed as a portion of time (from 0 to 1) over which a grid point is located in an eddy of the given sign. Bottom topography is for 1000, 2000, 3000 m (black contours), and for 2700 m (magenta contour). The 2700-m contour and Helgeland Ridge (its location is shown in Fig. 1) bound the area in the LB used for making the scatter plot in Fig. 13. (For interpretation of the references to color in this figure legend, the reader is referred to the web version of this article.)

occurrences of anticyclonic eddies (AE) and cyclonic eddies (CE) at a particular location, the mean eddy radius, and the orbital velocity, estimated using the "winding angle" method described in Section 2.5.

Displayed in Fig. 12 are the probabilities of AE (a) and CE (b) detection, which indicate the portion of time (out of unity) over which the point is located in an eddy of the given rotation. A strong maximum of AE probability (Fig. 12a) is observed in the area where the Lofoten Vortex resides (3–5°E, 69–70°N). Although the vortex exists permanently in EXP04 (after generation), the maximum probability reaches only about 0.8. This is the result of the vortex migration, which we address in the next section. The elevated values of the AE probability (0.2–0.4) extend over the northern and northeastern parts of the LB. This is a footprint of anticyclones that are generated in the eastern part of the basin due to the instability of the NwASC, then move westward and curl in a cyclonic direction. The probability of the CE detection is generally smaller that the probability of the AE detection, meaning that anticyclones are more frequent (Fig. 12b). The majority of CE in the LB is found on the periphery of the Lofoten Vortex as suggested by elevated values (0.2–0.3) of the CE probability around the time-mean vortex location. The generation of CE here is probably caused by the horizontal velocity shear between the vortex and the background cyclonic flow.

Our analysis suggests that not only are AE more frequent than CE in the LB, but also the former are usually stronger than the latter. To demonstrate this, we present a scatter diagram of the eddy radius versus the maximum eddy orbital velocity for the area bounded by the 2700 m isobath in the LB (Fig. 13; the 2700-m isobaths is drawn in Fig. 12). The larger eddies are characterized by stronger orbital velocities. For the given range of radiuses (10–70 km) the average orbital velocity for CE varies from 10 to 30 cm s^{-1}, while the average orbital velocity for AE varies between about 10 and 45 cm s^{-1}. The fact that anticyclones are more frequent, larger, and stronger than cyclones suggests that they should have a stronger impact on the Lofoten Vortex.

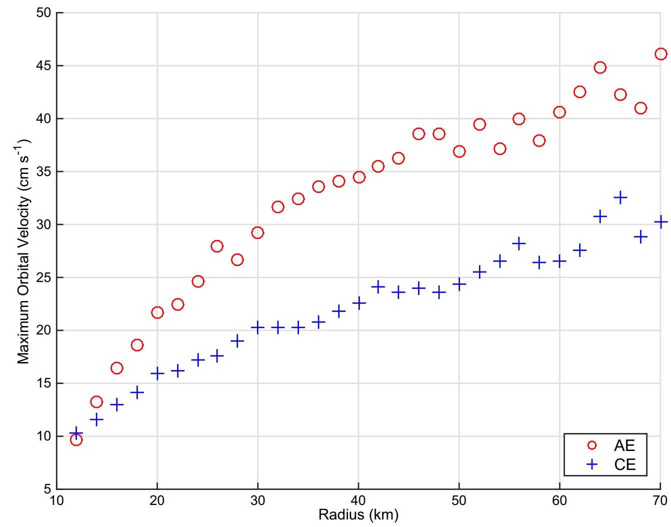

Fig. 13. Scatter plot of eddy radii versus corresponding values of the maximum eddy orbital velocities for anticyclones (red circles) and cyclones (blue crosses), calculated over an area bounded by the 2700-m isobath (marked by the magenta contour in Fig. 12) and the Helgeland Ridge (the southwestern boundary of the LB, Fig. 1). The eddy radius and orbital velocities are computed from velocities at 95 m depth. Abbreviations: AE – anticyclonic eddies, CE – cyclonic eddies. (For interpretation of the references to color in this figure legend, the reader is referred to the web version of this article.)

The time-mean radius of eddies in the LB varies from 20 to 30 km (Fig. 14a). The largest radius (~25–40 km) is associated with the Lofoten Vortex. It should be noted that this local maximum is partly due to eddy merging events. At the beginning of the merging process, the two merging eddies form a common exterior anticyclonic cell with two distinct cores (e.g. Cerretelli and Williamson, 2003; Meunier et al., 2005). During this stage, the eddy detection algorithm returns the radius of the exterior cell, which is greater than the radius of the Lofoten Vortex itself. Nevertheless, the visual analysis shows that the vortex's radius can sometimes exceed 40 km when no merging is taking place.

The average orbital velocity of eddies in the LB also peaks at the location of the Lofoten Vortex exceeding 30 cm s^{-1} (Fig. 14b). Eddies in the other regions are weaker with orbital velocities of 10–20 cm s^{-1}. The spatial pattern of the eddy orbital velocities demonstrates a pathway along which the strongest eddies with velocities reaching about 15 cm s^{-1} propagate. As suggested by Fig. 14b, the strongest eddies are formed by the NwASC at around 70°N, start moving westward, then veer northwestward, and spin counterclockwise towards the center of the LB.

3.6. Drift and strength of the Lofoten vortex

As follows from Fig. 9c, the core of the Lofoten Vortex in EXP04, characterized by maximum velocities, is located at about 500 m depth. Therefore, we use the model's velocities at a depth level of 477 m to estimate the OW parameter to track the location of the core, as described in Section 2.5. The core of the vortex appears to be quite well defined by the OW parameter, because the dominance of the vortex's rotation over shear and stretch results in

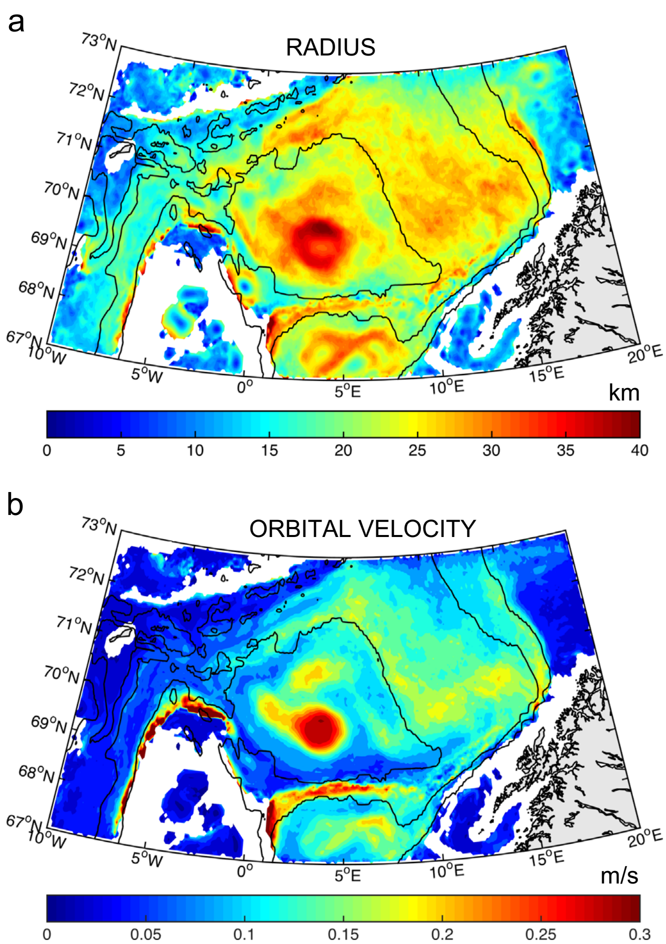

Fig. 14. The 1995–2012 mean (a) eddy radius (km) and (b) eddy orbital velocity ($m\,s^{-1}$). The eddy radius and orbital velocities are computed from velocities at 95 m depth. Bottom topography (black contours) is shown for 1000, 2000, and 3000 m.

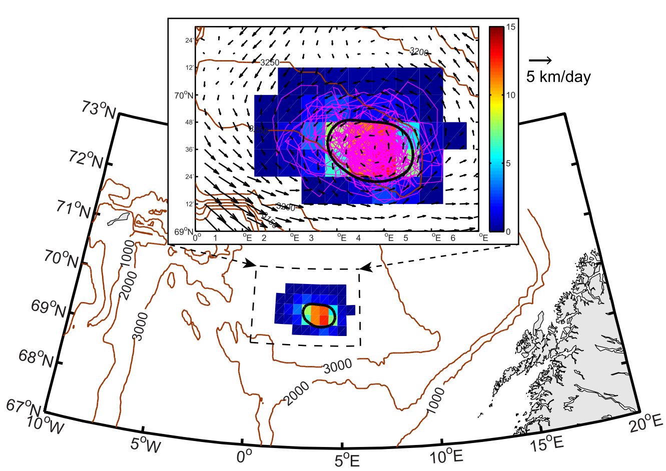

Fig. 15. The Lofoten Vortex (LV) locations, calculated from horizontal velocity components at 477 m depth (the location of the LV core in Fig. 9) simulated in EXP04. The insert panel is a zoom-in on the area bounded by the dashed rectangle in the main panel. The color scale shows the percentage of time over which the center of the LV is present in a particular square with dimensions 0.5° longitude and 0.2° latitude. The drift of the LV center is shown by the magenta curve. Arrows in the insert panel show the time mean eddy propagation velocities, calculated using the maximum cross-correlation method. The bold black contour is the $-0.1\times10^{-9}\,s^{-2}$ contour of the time-mean Okubo–Weiss parameter. (For interpretation of the references to color in this figure legend, the reader is referred to the web version of this article.)

strongly negative values of OW. The time-mean boundary of the vortex's core is shown by the closed black contour in Fig. 15. The drift of the vortex's center (Fig. 15, the magenta curve) is mainly restricted by the 3250-m isobath. Although the vortex movements are rather irregular, the average drift is cyclonic, which is confirmed by the maximum cross-correlation analysis of SSH fields and by visually inspecting the trajectories obtained from the OW fields. The average speed of the vortex's drift computed from its trajectory is 1.5 km/day, which agrees well with the approximately 1–2 km/day estimated by the maximum cross-correlation analysis (Fig. 15, insert). The location statistics of the vortex's center (Fig. 15, color scale) indicates that over 50% of the time the vortex resides in the southernmost part of the topographic depression with depths greater than 3250 m. It should be noted that the computed direction of the vortex's drift confirms the observational results of Ivanov and Korablev (1995a,b), Volkov et al. (2013), and Raj et al. (2015), but contradicts the results of Köhl (2007), who reported on an anticyclonic drift of the vortex.

Here, we calculate the strength of the Lofoten Vortex at each time step as the vertical component of relative vorticity averaged over its core (negative values). After the start of EXP04, the Lofoten Vortex is formed from an anticyclonic eddy that, after being generated by the NwAC, drifted to the interior of the LB. The eddy reached the center of the basin after about 220 days of integration. The strength of the Lofoten Vortex exhibits rapid short-period intensifications, seasonal and interannual variability (Fig. 16). The vortex is usually stronger in October–December; however, the amplitude of the seasonal cycle of the vortex strength ($1.8\times10^{-6}\,s^{-1}$) is only a third of the standard deviation of the signal ($5\times10^{-6}\,s^{-1}$). The long-term intensification of the vortex is probably related to the model spin-up. The record maximum of the vortex's strength was reached in winter 2002/2003. It is noteworthy that the interannual variability of the model-simulated strength of the Lofoten Vortex is similar to the interannual variability of the altimetry-derived eddy intensity (EKE averaged over the vortex's area) in Raj et al. (2015, see their Fig. 9), suggesting that physics behind the variability of the vortex in the model is realistic.

The visual analysis of the model velocity maps (see supplementary online material, SM 1) suggests that short-period intensifications of the Lofoten Vortex occur due to mergers with anticyclonic eddies, which is consistent with the hypothesis of Köhl (2007). Two examples of such mergers are illustrated in Figs. 17 and 18, showing the evolution of the relative vorticity fields and the relative vorticity of the vortex's core (zoom-in view is shown on periods marked by the magenta stripes in Fig. 16). Both mergers lead to strengthening of the vortex. It is interesting

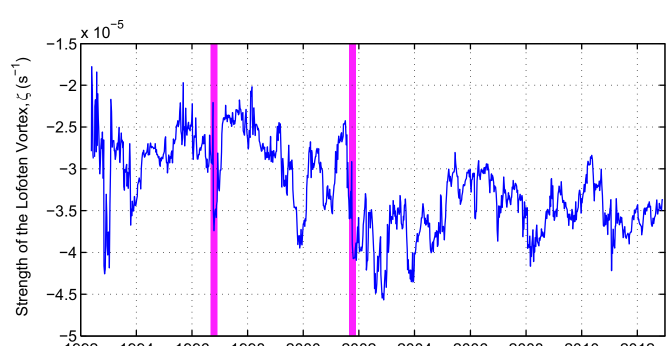

Fig. 16. Strength of the Lofoten Vortex expressed as the relative vorticity (s^{-1}) averaged over the area within the boundary of the vortex core at 477 m depth. Magenta stripes mark the periods of the vortex strengthening illustrated in Figs. 17 and 18. (For interpretation of the references to color in this figure legend, the reader is referred to the web version of this article.)

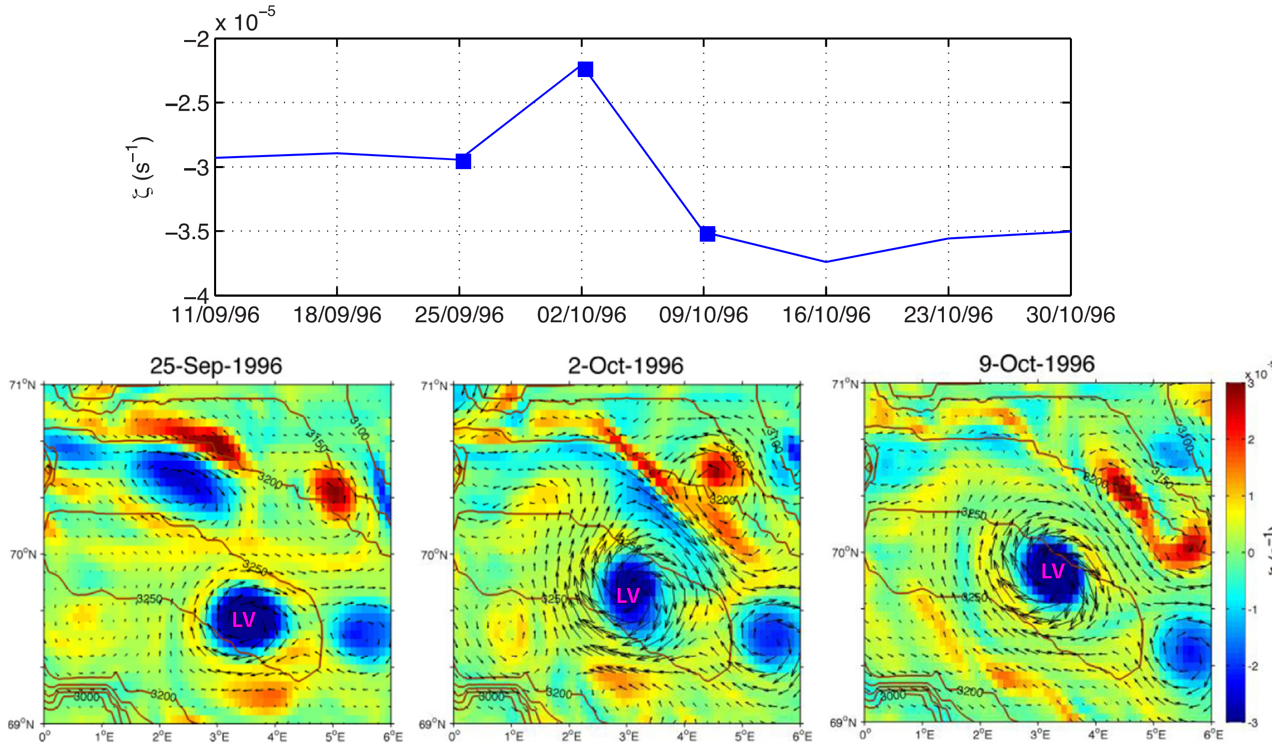

Fig. 17. A zoom-in of the Lofoten Vortex strength (top) from Fig. 14 and the evolution of the velocity (arrows) and vorticity (color, s^{-1}) fields at 477 m depth (bottom). This figure illustrates a merging event of the Lofoten Vortex (marked by LV) with an anticyclonic eddy and the subsequent strengthening of the former. The time interval corresponds to the left magenta stripe in Fig. 16. (For interpretation of the references to color in this figure legend, the reader is referred to the web version of this article.)

to note that at the first stage of the merging process, the Lofoten Vortex weakens, as was observed on October 2, 1996 (Fig. 17) and on September 26, 2001 (Fig. 18). This is possibly because (i) at the first stage of the merging process some energy is spent on the formation of the exterior circulation cell that envelops both eddies (Cerretelli and Williamson, 2003; Meunier et al., 2005); and (ii) as the merging starts, the area over which the mean vorticity is calculated becomes larger, including the incoming (and often weaker) eddy.

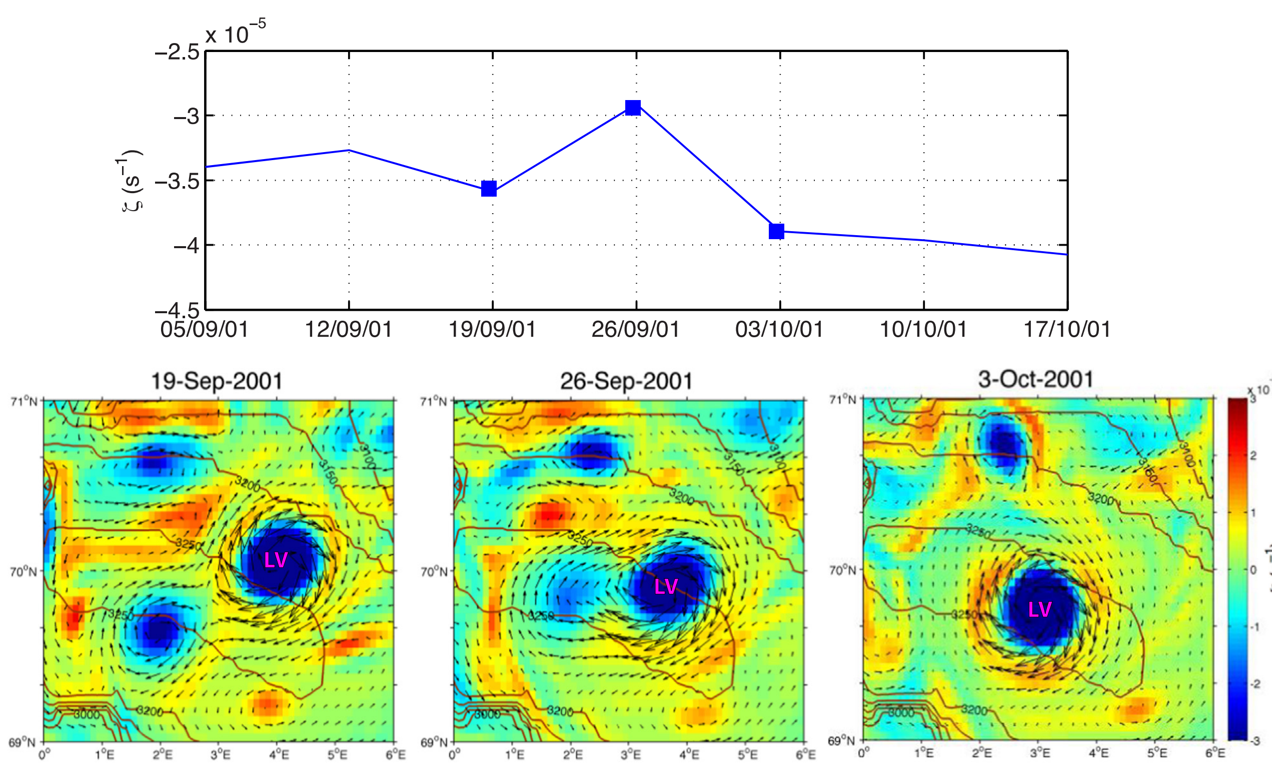

Fig. 18. (For interpretation of the references to color in this figure legend, the reader is referred to the web version of this article.)Same as Fig. 17, but for another time interval, marked by the right magenta stripe in Fig. 16.

3.7. Forcing of the depth-integrated flow

As has been demonstrated above, the Lofoten Vortex has a strong barotropic component. The mean orbital velocities near the bottom in EXP04 reach 5 cm s^{-1}. This means that we can estimate the barotropic vorticity budget components in order to investigate what processes drive the depth-integrated flow around the vortex. Based on the derived locations of the Lofoten Vortex (Fig. 15), the barotropic vorticity budget is analyzed over the area A bounded by 1.5°E–5.5°E and 69.2°N–70.2°N. The analysis below is similar to the one carried out by Volkov and Fu (2008) to study the dynamics of the Zapiola Anticyclone in the Argentine Basin. The barotropic vorticity equation for the depth-integrated flow can be expressed as follows:

$$\frac{\partial\zeta}{\partial t} = -\mathbf{u}\nabla\zeta - \beta v + \frac{(\zeta+f)}{H}\left(\frac{\partial\eta}{\partial t} + \mathbf{u}\nabla H\right) + \frac{1}{\rho}\nabla\times\left(\frac{\boldsymbol{\tau}}{H}\right) - D \quad (1)$$

where $\mathbf{u}(u, v)$ is the depth-integrated velocity vector, f is the planetary vorticity, $\beta = \partial f/\partial y$ is the meridional gradient of planetary vorticity, H is the depth, η is the sea level anomaly relative to the time mean, ρ is the density, and $\boldsymbol{\tau}(\tau_x, \tau_y)$ is the wind stress vector. The residual D includes the integral dissipative force and the impact of intra-weekly variability of velocity fields. Using the output of EXP04, we estimated all the terms of the Eq. (1), except D, and integrated them over the area A. The terms on the right hand side of Eq. (1), that balance the time change of the relative vorticity over A, are (from left to right): (i) the advection of the relative vorticity gradient; (ii) the advection of the planetary vorticity gradient; (in brackets) (iii) the generation of vorticity due to the stretching of the water column and (iv) the advection of vorticity induced by bottom topography (topographic effect); (v) the forcing by wind stress (wind stress is part of the model output); and (vi) the residual.

Table 1 presents correlation coefficients (r) between $\partial\zeta/\partial t$ and the terms on the RHS of Eq. (1). The 95% significance level for correlation, shown in brackets, was estimated by computing correlations between the pairs of 5000 Monte Carlo simulations of random time series that have the same degrees of freedom (the number of independent samples) as the original model-derived time series (accounting for autocorrelations). The number of independent samples, N^*, was determined using a formula of Leith (1973): $N* = -\frac{N}{2} ln[r(\Delta t)]$, where N is the number of data points in the time series and $r(\Delta t)$ is the one-lag autocorrelation.

The time change of the relative vorticity ($\partial\zeta/\partial t$) is well balanced by the terms on the right hand side (RHS) of Eq. (1) without D (Fig. 19a). The correlation between $\partial\zeta/\partial t$ and the RHS terms without D is 0.8, the significance of which is well above the 95% confidence. The residual D is sizable, but uncorrelated with $\partial\zeta/\partial t$ (r=0.06). The individual RHS terms of Eq. (1) are shown in Fig. 19b and c. It appears that the advection of the relative vorticity gradient, $-\mathbf{u}\nabla\zeta$, makes the major contribution to $\partial\zeta/\partial t$ (Fig. 19b, red curve). The correlation between $\partial\zeta/\partial t$ and $-\mathbf{u}\nabla\zeta$ is 0.75. The impact of vortex stretching is negligible (not shown), because this term is more than two orders of magnitude smaller than the other terms. This means that changes in the height of the water column caused by wind-driven divergence and/or buoyancy forcing do not significantly contribute to $\partial\zeta/\partial t$. Nevertheless, the fact that this result is valid for the area of integration around the Lofoten Vortex does not imply that buoyancy forcing does not affect the vortex itself. The correlation between $\partial\zeta/\partial t$ and the advection of the planetary vorticity (Fig. 19b, blue curve) is at the edge of significance (r=0.07). The topographic and wind stress terms (Fig. 19c, blue and red curves, respectively) are significantly correlated with $\partial\zeta/\partial t$ (Table 1), but make a small contribution compared to $-\mathbf{u}\nabla\zeta$.

Table 1
Correlation coefficients between the time change of relative vorticity and the RHS terms of Eq. (1) integrated over the area A (1.5°E–5.5°E and 69.2°N–70.2°N). The 95% significance level is shown in brackets and significant correlations are shown in bold.

	RHS of Eq. (1) except D	$-\mathbf{u}\nabla\zeta$	$-\beta v$	$\frac{(\zeta+f)}{H}(\mathbf{u}\nabla H)$	$\frac{1}{\rho}\nabla\times(\frac{\boldsymbol{\tau}}{H})$
$\partial\zeta/\partial t$	**0.80** (0.06)	**0.75** (0.06)	0.07 (0.07)	**0.19** (0.08)	**0.10** (0.06)

The advection of the relative vorticity gradient can be decomposed into the components associated with the mean flow and with the time-dependent (or eddy) flow:

$$\mathbf{u}\cdot\nabla\zeta = \bar{\mathbf{u}}\cdot\nabla\bar{\zeta} + \bar{\mathbf{u}}\cdot\nabla\zeta' + \mathbf{u}'\cdot\nabla\bar{\zeta} + \mathbf{u}'\cdot\nabla\zeta' \quad (2)$$

where $\mathbf{u} = \bar{\mathbf{u}} + \mathbf{u}'$ and $\zeta = \bar{\zeta} + \zeta'$. The first term on the right side of Eq. (2) is time independent and does not contribute to $\partial\zeta/\partial t$. The second term is the advection of the vorticity gradient anomaly by the mean flow. The last two terms are the advection of the mean vorticity gradient and the vorticity gradient anomaly by the eddy flow, respectively. Since we use weekly model output, it is impossible to accurately estimate the last term of (2), as the impact of intra-weekly variability of the velocity field is not accounted for. However, the disregard of the intra-weekly variability does not change our conclusion that the advection of the relative vorticity gradient is the main driver for the variability of ζ over the area A. The correlation coefficients between the last three terms of Eq. (2) and $\mathbf{u}\nabla\zeta$ / $\partial\zeta/\partial t$ are shown in Table 2. One can see that eddy flow makes the major contribution to $\mathbf{u}\nabla\zeta$, in particular, the advection of the vorticity gradient anomaly by the eddy flow ($\mathbf{u}'\nabla\zeta'$). The correlation between $\mathbf{u}\nabla\zeta$ and $\mathbf{u}'\nabla\zeta'$ is 0.85, while the correlation between $\mathbf{u}\nabla\zeta$ and $\bar{\mathbf{u}}\nabla\zeta'/\mathbf{u}'\nabla\bar{\zeta}$ is 0.24/0.34. The correlation between $\partial\zeta/\partial t$ and $-\mathbf{u}'\nabla\zeta'$ is 0.7, while the correlation between $\partial\zeta/\partial t$ and $-\bar{\mathbf{u}}\nabla\zeta'/-\mathbf{u}'\nabla\bar{\zeta}$ is much smaller (r=0.11/0.19), but significant at 95% confidence. These results support the findings of Köhl (2007), who first suggested the importance of eddy fluxes in the generation and stability of the Lofoten Vortex.

The vortex interacts with a cyclonic flow around the center of the LB and with the background cyclonic propagation of eddies. It is, therefore, interesting to understand where the relative vorticity influencing the variability of the vortex's strength is advected from. The advection of the relative vorticity gradient integrated over the area A can be computed as the sum of the integrals of the relative vorticity fluxes across western (w), eastern (e), southern (s), and northern (n) boundaries of A plus the divergence of ζ integrated over A:

$$-\iint_A \mathbf{u}\cdot\nabla\zeta dxdy = \int_s^n u_w\zeta_w dy - \int_s^n u_e\zeta_e dy + \int_w^e v_s\zeta_s dx - \int_w^e v_n\zeta_n dx + \iint_A \zeta\nabla\mathbf{u} dxdy \quad (3)$$

The u and v flux terms are positive in the eastward and northward directions, respectively. The last term of Eq. (3), the divergence of ζ, is small compared to the first four terms (Fig. 20a, black curve). The standard deviation of the divergence term ($\approx 6\times10^{-4}$ m^2 s^{-2}) is almost an order of magnitude smaller than the standard deviations of the relative vorticity flux terms ($\approx$ 4–5 $\times 10^{-3}$ m^2 s^{-2}). Therefore, the flow can be regarded as almost non-divergent and the divergence term in Eq. (3) can be neglected. One can see that vorticity fluxes across all four boundaries make significant contributions to the area integrals of $\mathbf{u}\nabla\zeta$ and $\partial\zeta/\partial t$ (Fig. 20 and Table 3). However, the western (Fig. 20a) and northern (Fig. 20d) boundaries appear to be more important as the correlations between $\partial\zeta/\partial t$ and vorticity fluxes across these boundaries (r=0.4) are stronger than the correlations between $\partial\zeta/\partial t$ and vorticity fluxes across the eastern (r=0.16, Fig. 20b) and southern (r=0.21, Fig. 20c) boundaries. The magnitude of correlations is

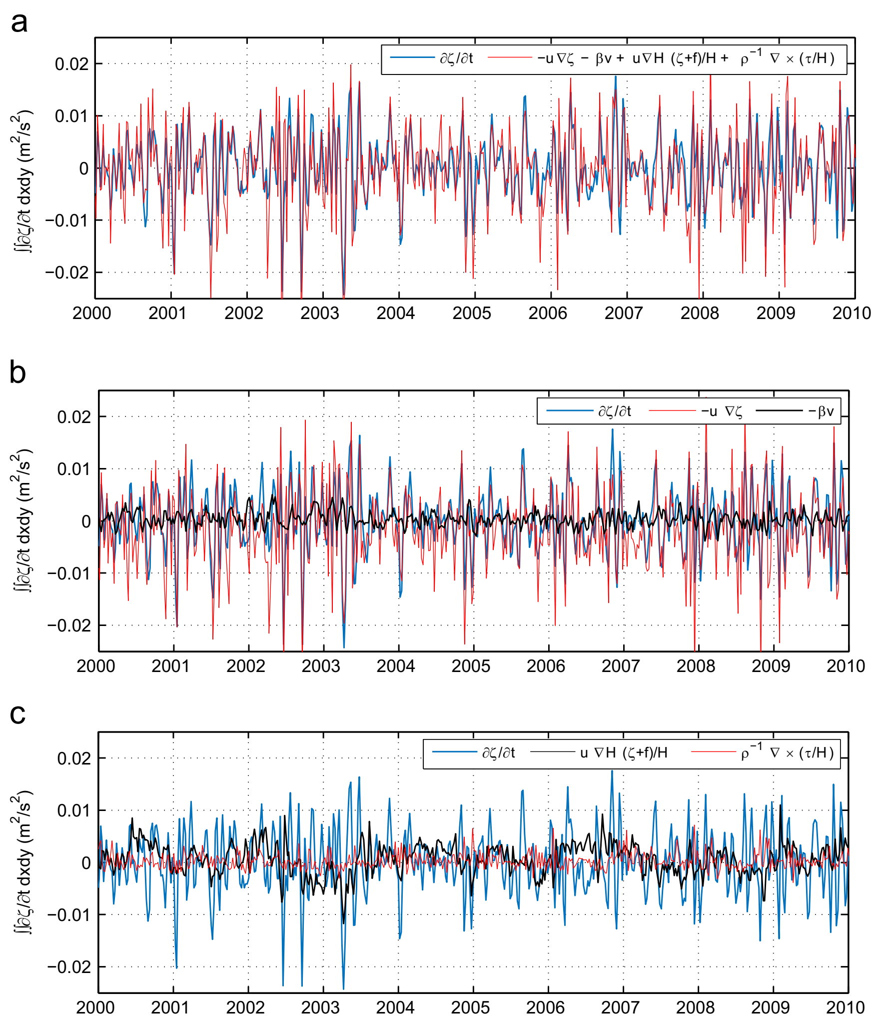

Fig. 19. The terms of the Eq. (1), integrated over the area 1.5°E–5.5°E, 69.2°N–70.2°N: the time change of the relative vorticity (blue curves) versus (a) the sum of the right hand side terms minus the residual D (red curve), (b) the advection of the relative and planetary vorticity gradients (red and black curves, respectively), (c) the advection of vorticity induced by bottom topography (black curve) and forcing by wind stress (red curve). For clarity, only 10 years of the model run are shown. The correlation coefficients between these terms, calculated over the entire period of the model run, are presented in Table 1. (For interpretation of the references to color in this figure legend, the reader is referred to the web version of this article.)

Table 2
Correlation coefficients between the advection of the relative vorticity gradient (and $\partial\zeta/\partial t$) and the RHS terms of Eq. (2) integrated over the area A (1.5°E–5.5°E and 69.2°N–70.2°N). The 95% significance level is shown in brackets and significant correlations are shown in bold.

	$-\bar{\mathbf{u}}\nabla\zeta'$	$-\mathbf{u}'\nabla\bar{\zeta}$	$-\mathbf{u}'\nabla\zeta'$
$-\mathbf{u}\nabla\zeta$	**0.24** (*0.06*)	**0.34** (*0.06*)	**0.85** (*0.06*)
$\partial\zeta/\partial t$	**0.11** (*0.07*)	**0.19** (*0.07*)	**0.70** (*0.06*)

consistent with the sense of eddy propagation in the LB. Because eddies propagate counterclockwise around the center of the basin, the number of eddies crossing the boundaries of A, and, consequently, the relative importance of each boundary, is expected to decrease in the counterclockwise direction as well.

4. Summary and conclusions

The warm and saline Atlantic waters that constitute an important part of the upper limb of the Atlantic Meridional Overturning Circulation undergo transformation as they transit the LB – a topographic depression adjacent to the Greenland Sea. The basin serves as a large heat reservoir and accounts for a substantial fraction of the surface buoyancy loss in the Nordic Seas (Björk et al., 2001; Nilsen and Falck, 2006; Rossby et al., 2009a). Despite its potential importance in the global climate system (Richards and Straneo, 2015), our knowledge of the local dynamical mechanisms is still limited. The most prominent dynamical feature of the LB is a quasi-permanent anticyclonic vortex, discovered in the 20th century and since then repeatedly confirmed by modern instruments and observational systems, including drifters and satellite altimetry, and by ocean model simulations. Two hypotheses for the vortex formation and stability have been proposed: (i) the regeneration of density anomaly by winter convection accompanied by the reinforcement of the vortex (Ivanov and Korablev, 1995a and 1995b) and (ii) the merging of anticyclonic eddies (Köhl, 2007).

In this study, we have revisited the problem of the Lofoten Vortex formation by conducting and analyzing three numerical experiments using a high-resolution eddy-permitting ocean model. The experiments were identical in terms of initial and boundary conditions, forcing, and control parameters, and differed in spatial resolution only. It appears that the dynamics of the LB is very sensitive to the horizontal resolution. The main difference between the low-resolution run (average grid spacing = 18 km) and the higher resolution runs (average grid spacing = 9 and 4 km,

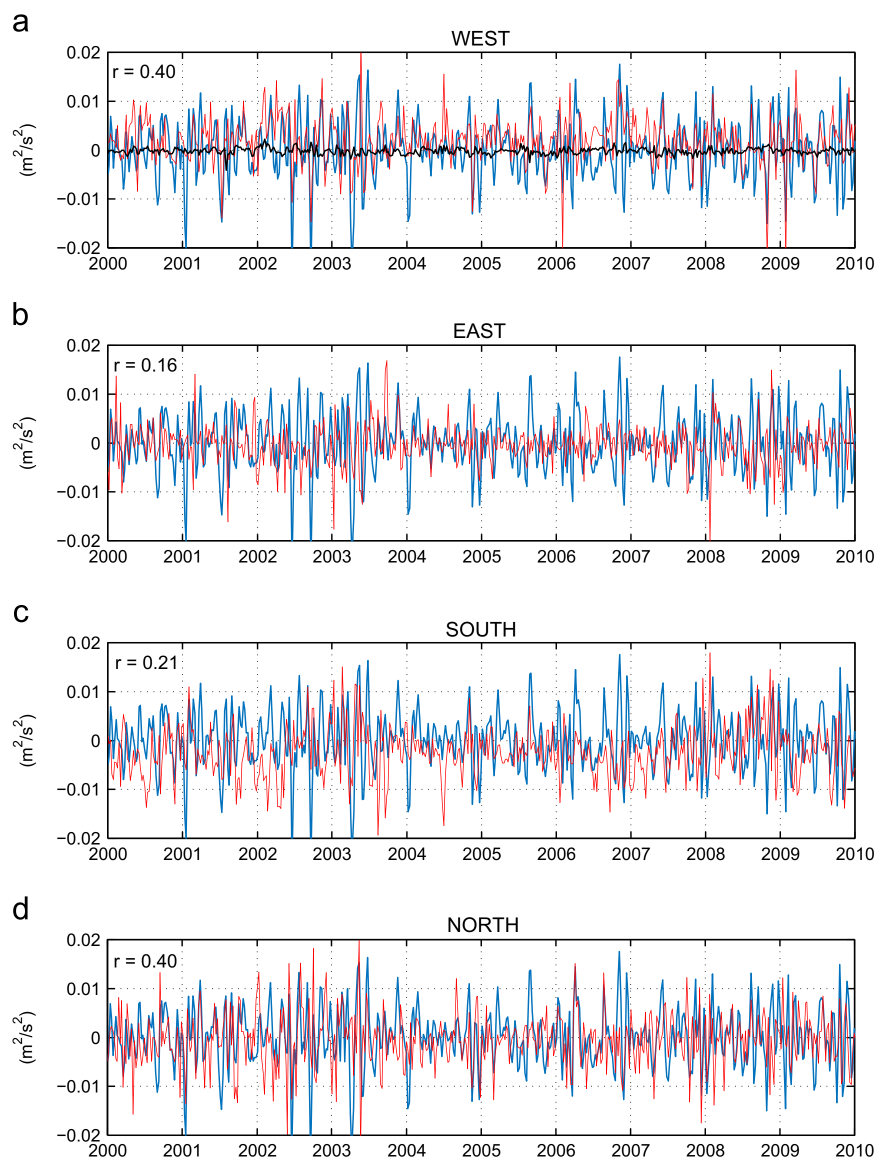

Fig. 20. Relative vorticity fluxes integrated over the western (a), eastern (b), southern (c), and northern (d) boundaries of the area 1.5°E–5.5°E, 69.2°N–70.2°N (red curves), within which the Lofoten Vortex resides, and the area-integral of the time change of the relative vorticity (blue curves). The black curve in (a) is the divergence of the relative vorticity (the last term of Eq. (3)). For clarity, only 10 years of the model run are shown. Correlation coefficients, calculated over the entire period of the model run, are shown in Table 3. (For interpretation of the references to color in this figure legend, the reader is referred to the web version of this article.)

Table 3
Correlation coefficients between the advection of the relative vorticity gradient (and $\partial\zeta/\partial t$) integrated over the area A (1.5°E–5.5°E and 69.2°N–70.2°N) and the fluxes of relative vorticity across the area boundaries (Eq. (3)). The 95% significance level is 0.06 for all correlations.

	$\int_s^n u_w \zeta_w dy$	$-\int_s^n u_e \zeta_e dy$	$\int_w^e v_s \zeta_s dx$	$-\int_w^e v_n \zeta_n dx$
$-\iint_A \mathbf{u}\cdot\nabla\zeta dx dy$	0.44	0.21	0.42	0.47
$\partial\zeta/\partial t$	0.40	0.16	0.21	0.40

respectively) is the formation of sea level depression and associated cyclonic circulation in the LB and in the adjacent Norwegian Basin in the latter. It takes about a year of the model run for the cyclonic flow to establish (Fig. 6). The halving of the horizontal grid spacing in each consecutive experiment also led to an increase of current velocities (Fig. 5), EKE (Fig. 7), and the speed of eddy propagation (Fig. 11).

The Lofoten Vortex is formed only in the higher resolution runs (Figs. 5, 8 and 9) and best represented in the 4-km experiment. This experiment better simulates the mesoscale eddy variability, which is reflected in a more realistic (compared to observations) distribution of EKE (Fig. 7). It should be noted that only the resolution of the 4-km experiment is significantly smaller than the Rossby radius of deformation in the LB (20–25 km). This result thus provides an experimental evidence of the importance of eddies in the formation and stability of the vortex. In the 4-km run, the Lofoten Vortex is formed from an anticyclonic eddy that separated from the NwASC and reached the center of the LB after about 220 days of the model run. Then the vortex is maintained by anticyclonic eddies that are generated by the NwASC, and propagate along a cyclonic path towards the center of the LB. Some of the eddies merge with the vortex and reinforce it.

Most eddies present in the LB have radii of 20–30 km (Fig. 14). The Lofoten Vortex has the largest radius, sometimes exceeding 40 km, which agrees well with the altimetry-based results of Raj et al. (2015). We have shown that anticyclonic eddies in the LB are usually more frequent and intense than cyclonic eddies (Fig. 12).

The largest probability of anticyclonic eddy occurrence is observed near the time-mean position of the Lofoten Vortex (up to 80% of time) and along the preferred path of anticyclonic eddy propagation in the northern and northeastern parts of the LB (20–40% of time). The largest probability of the cyclonic eddy occurrence (20–30% of time) is observed on the periphery of the Lofoten Vortex, probably due to the shear between the vortex's orbital velocity and the background flow. The maximum orbital velocity for cyclones varies from 10 to 30 cm s^{-1}, while the maximum orbital velocity for anticyclones is 10–45 cm s^{-1} (Fig. 13).

The average orbital velocity of eddies reaches 30–40 cm s^{-1} at the location of the Lofoten Vortex. As already documented in previous studies, the Lofoten Vortex is not stationary. Our model results have shown that it generally stays within the region 1.5°E–5.5°E and 69.2°N–70.2°N (Fig. 15). The average drift of the vortex is cyclonic with a speed of 1.5 km day^{-1}, which is opposite to the direction reported by Köhl (2007), but confirms the observational results of Ivanov and Korablev (1995a,b), Volkov et al. (2013), and Raj et al. (2015). The strength of the vortex is subject to synoptic, seasonal, and interannual variability (Fig. 16). The short-period intensifications are related to eddy merging events. Confirming the model-based findings of Köhl (2007) and remote sensing study of Raj et al. (2015), we have demonstrated that anticyclonic eddies merge with the Lofoten Vortex and contribute to its intensification. We have noted that when an anticyclonic eddy approaches the Lofoten Vortex, the latter weakens just before the merging takes place and then strengthens after the merging. The initial weakening is probably due to the energy spent for the formation of the exterior anticyclonic cell at the beginning of the merging process.

Because the time-mean circulation in the LB and the Lofoten Vortex itself in the model is to a large degree barotropic, we have analyzed the barotropic vorticity budget to investigate the mechanisms driving the variability of the relative vorticity integrated over the area where the vortex resides (1.5°E–5.5°E and 69.2°N–70.2°N). The analysis has revealed that the advection of the relative vorticity gradient by eddies is the major mechanism that drives the variability of the relative vorticity inside the area. The advection across the northern and western boundaries of the domain, within which the Lofoten Vortex resides, is found to be particularly important. The relative contributions of the other mechanisms, such as the advection of the planetary vorticity gradient, local wind forcing, the advection of vorticity induced by the bottom topography (the topographic effect), and vortex stretching, are rather small or unimportant. The vortex stretching includes divergence and buoyancy forcing, which are found to be negligible. In summary, the results of our study confirm the importance of eddies in the formation and stability of the Lofoten Vortex and show that the variability of the vortex is mostly driven by eddy vorticity fluxes.

Acknowledgments

This research was funded by the NASA Physical Oceanography program (Grant NNX11AE27G) and partially supported by the base funds of NOAA Atlantic Oceanographic and Meteorological Laboratory (USA) and Saint Petersburg State University (Russia). We gratefully acknowledge computational resources and support from the NASA Advanced Supercomputing (NAS) Division. The ECCO2 global ocean model output is provided by the ECCO2 project (http://ecco2.jpl.nasa.gov). A. Koubryakov was supported through a postdoctoral research Grant 18.50.1059.2014 from Saint Petersburg State University (Russia). We thank three anonymous reviewers for constructive remarks and helpful suggestions. We are also grateful to Dr. Marlos Goes, Dr. Elizabeth Johns for reading and commenting on the initial version of the manuscript.

Appendix A. Supplementary Information

Supplementary data associated with this article can be found in the online version at http://dx.doi.org/10.1016/j.dsr.2015.09.001.

References

Adcroft, A., Hill, C., Marshall, J., 1997. The representation of topography by shaved cells in a height coordinate model. Mon. Weather Rev. 125, 2293–2315.
Alexeev, G.V., Bagryantsev, M.V., Bogorodsky, P.V., Vasin, V.B., Shirokov, P.E., 1991. Structure and circulation of water masses in the area of an anticyclonic vortex in the north-eastern part of the Norwegian Sea. Russian Problems of Arctic and Antarctic. vol. 65, Gidrometeoizdat, Leningrad.
Andersson, M., LaCasce, J.H., Koszalka, I., Orvik, K.A., Mauritzen, C., 2011. Variability of the Norwegian Atlantic current and associated eddy field from surface drifters. J. Geophys. Res. 116, C08032. http://dx.doi.org/10.1029/2011JC007078.
Antonov, J. I., D. Seidov, T. P. Boyer, R. A. Locarnini, A. V. Mishonov, H. E. Garcia, O. K. Baranova, M. M. Zweng, and D. R. Johnson, 2010. *World Ocean Atlas 2009, Volume 2: Salinity.* S. Levitus, Ed. NOAA Atlas NESDIS 69, U.S. Government Printing Office, Washington, D.C., 184 pp.
Björk, G., Gustafsson, B.G., Stigebrandt, A., 2001. Upper layer circulation of the Nordic seas as inferred from the spatial distribution of heat and freshwater content. Polar Res. 20, 161–168.
Blindheim, J., Rey, F., 2004. Water–mass formation and distribution in the Nordic seas during the 1990s ICES. J. Mar. Sci. 61, 846–863.
Cerretelli, C., Williamson, C.H.K., 2003. The physical mechanism for vortex merging. J. Fluid Mech. 475, 41–77.
Chaigneau, A., Gizolme, A., Grados, C., 2008. Mesoscale eddies off Peru in altimeter records: identification algorithms and eddy spatio-temporal patterns. Prog. Oceanogr. 79 (106–119), 2008.
Chelton, D.B., de Szoeke, R.A., Schlax, M.G., El Naggar, K., Siwertz, N., 1998. Geographical variability of the first-baroclinic Rossby radius of deformation. J. Phys. Oceanogr. 28, 433–460.
Fu, L.-L., 2006. Pathways of eddies in the South Atlantic Ocean revealed from satellite altimeter observations. Geophys. Res. Lett. 33, L14610. http://dx.doi.org/10.1029/2006GL026245.
Fu, L.-L., 2009. Pattern and velocity of propagation of the global ocean eddy variability. J. Geophys. Res. 114, C11017. http://dx.doi.org/10.1029/2009JC005349.
Ikeda, M., Johannessen, J.A., Lygre, K., Sandven, S., 1989. A process study of mesoscale meanders and eddies in the Norwegian Coastal current. J. Phys. Oceanogr. 19, 20–35.
Ivanov, V.V., Korablev, A.A., 1995a. Formation and regeneration of the pycnocline lens in the Norwegian Sea. Russ. Meteor. Hydrol. 9, 62–69.
Ivanov, V.V., Korablev, A.A., 1995b. Dynamics of an intrapycnocline lens in the Norwegian Sea. Russ. Meteor. Hydrol. 10, 32–37.
Isern-Fontanet, J., García-Ladona, E., Font, J., 2006. Vortices of the Mediterranean Sea: An Altimetric Perspective. J. Phys. Oceanogr. 36, 87–103. http://dx.doi.org/10.1175/JPO2826.1.
Isern-Fontanet, J., García-Ladona, E., Font, J., 2003. Identification of marine eddies from altimetry. J. Atmos. Ocean Technol. 20, 772–778.
Johannessen, J.A., Svendsen, E., Sandven, S., Johannessen, O.M., 1989. Three-dimensional structure of mesoscale eddies in the Norwegian Coastal Current. J. Phys. Oceanogr. 19, 3–19.
Koszalka, I., LaCasce, J.H., Andersson, M., Orvik, K.A., Mauritzen, C., 2011. Surface circulation in the Nordic seas from clustered drifters. Deep-Sea Res. I 58, 468–485.
Kubryakov, A.A., Stanichny, S.V., 2015. Mesoscale eddies in the Black Sea from altimetry data. Oceanology 55 (Suppl. 1), S1–S13.
Köhl, A., 2007. Generation and stability of a quasi-permanent vortex in the Lofoten Basin. J. Phys. Oceanogr. 37, 2637–2651. http://dx.doi.org/10.1175/2007JPO3694.
Large, W.G., McWilliams, J.C., Doney, S.C., 1994. Oceanic vertical mixing: a review and a model with a nonlocal boundary layer parameterization. Rev. Geophys. 32, 363–403.
Leith, C.E., 1973. The standard error of time-averaged estimates of climatic means. J. Appl. Meteorol. 12, 1066–1069.
Le Traon, P.-Y., Nadal, F., Ducet, N., 1998. An improved mapping method of multisatellite altimeter data. J. Atmos. Oceanic Technol. 15, 522–534.
Locarnini, R.A., Mishonov, A.V., Antonov, J.I., Boyer, T.P., Garcia, H.E., Baranova, O.K., Zweng, M.M., Johnson, D.R., 2010. World Ocean Atlas. In: Levitus, S. (Ed.), Temperature Vol. 1. NOAA Atlas NESDIS 68, U.S. Government Printing Office, Washington, D.C., p. 184.
Losch, M., Menemenlis, D., Heimbach, P., Campin, J.-M., Hill, C., 2010. On the formulation of sea-ice models. Part 1: Effects of different solver implementations and parameterizations. Ocean Model. 33, 129–144.
Lumpkin, R., Johnson, G.C., 2013. Global ocean surface velocities from drifters:

mean, variance, ENSO response, and seasonal cycle. J. Geophys. Res. 118, 2992–3006. http://dx.doi.org/10.1002/jgrc.20210.
Marshall, J., Adcroft, A., Hill, C., Perelman, L., Heisey, C., 1997. A finite volume, incompressible Navier–Stokes model for studies of the ocean on parallel computers. J. Geophys. Res. 102, 5753–5766. http://dx.doi.org/10.1029/96JC02775.
Maximenko, N., Niiler, P., Centurioni, L., Rio, M.-H., Melnichenko, O., Chambers, D., Zlotnicki, V., Galperin, B., 2009. Mean dynamic topography of the ocean derived from satellite and drifting buoy data using three different techniques. J. Atmos. Ocean. Technol. 26, 1910–1919.
Menemenlis, D., Campin, J., Heimbach, P., Hill, C., Lee, T., Nguyen, A., Schodlok, M., Zhang, H., 2008. ECCO2: High resolution global ocean and sea ice data synthesis. Mercat. Ocean Q. Newsl. 31, 13–21.
Menemenlis, D., Fukumori, I., Lee, T., 2005. Using Green's functions to calibrate an ocean general circulation model. Mon. Wea. Rev. 133, 1224–1240.
Meunier, P., Le Dizes, S., Leweke, T., 2005. Physics of vortex merging. Comptes Rendus Physique 6. Elsevier, pp. 431–450, n 4–5.
Morrow, R., Birol, F., Griffin, D., Sudre, J., 2004. Divergent pathways of cyclonic and anti-cyclonic ocean eddies. Geophys. Res. Lett. 31, L24311. http://dx.doi.org/10.1029/2004GL020974.
Nguyen, A.T., Menemenlis, D., Kwok, R., 2011. Arctic ice-ocean simulation with optimized model parameters: approach and assessment. J. Geophys. Res. 116, C04025. http://dx.doi.org/10.1029/2010JC006573.
Niiler, P.P., Paduan, J.D., 1995. Wind-driven motions in the northeast Pacific as measured by Lagrangian drifters. J. Phys. Oceanogr. 25, 2819–2830.
Nilsen, J.E.O., Falck, E., 2006. Variation of mixed layer properties in the Norwegian Sea for the period 1948–1999. Progr. Oceanogr. 70, 58–90.
Pazan, S.E., Niiler, P.P., 2000. Recovery of near-surface velocity from undrogued drifters. J. Atmos. Ocean. Technol. 18, 476–489.
Okubo, A., 1970. Horizontal dispersion of floatable particles in the vicinity of velocity singularities such as convergences. Deep Sea Res. 17, 445–454.
Poulain, P.-M., Warn-Varnas, A., Niiler, P.P., 1996. Near-surface circulation of the Nordic seas as measured by Largangian drifters. J. Geophys. Res. 101 (C8), 18237–18258.
Raj, R.P., Chafik, L., Even, J., Nilsen, O., Eldevik, T., Halo, I., 2015. The Lofoten Vortex of the Nordic Seas. Deep-Sea Res. I 96, 1–14.
Richards, C.G., Straneo, F., 2015. Observations of water mass transformation and eddies in the Lofoten Basin of the Norwegian Seas. J. Phys. Oceanogr. 45, 1735–1756. http://dx.doi.org/10.1175/JPO-D-14-0238.1.
Rossby, T., Ozhigin, V., Ivshin, V., Bacon, S., 2009a. An isopyncal view of the Nordic seas hydrography with focus on properties of the Lofoten Basin. Deep-Sea Res. I 56, 1955–1971.
Rossby, T., Prater, M.D., Søiland, H., 2009b. Pathways of inflow and dispersion of warm waters in the Nordic seas. J. Geophys. Res. 114, C04011. http://dx.doi.org/10.1029/2008JC005073.
Sadarjoen, A., Post, F.H., 2000. Detection, quantification, and tracking of vortices using streamline geometry. Vis. Comput. Graph. 24, 333–341.
Segtnan, O.H., Furevik, T., Jenkins, A.D., 2011. Heat and freshwater budgets of the Nordic Seas computed from atmospheric reanalysis and direct ocean observations. J. Geophys. Res. 116 (C11003). http://dx.doi.org/10.1029/2011JC006939.
Smith, W.H.F., Sandwell, D.T., 1997. Global sea floor topography from satellite altimetry and ship depth soundings. Science 277 (5334), 1956–1962.
Søiland, H., Rossby, T., 2013. On the structure of the Lofoten Basin Eddy. J. Geophys. Res. Oceans 118, 4201–4212. http://dx.doi.org/10.1002/jgrc.20301.
Volkov, D.L., Belonenko, T.V., Foux, V.R., 2013. Puzzling over the dynamics of the Lofoten Basin – a sub-Arctic hot spot of ocean variability. Geophys. Res. Lett. 40 (4), 738–743. http://dx.doi.org/10.1002/grl.50126.
Volkov, D.L., Pujol, M.-I., 2012. Quality assessment of a satellite altimetry data product in the Nordic, Barents, and Kara seas. J. Geophys. Res. 117, C03025. http://dx.doi.org/10.1029/2011JC007557.
Volkov, D.L., Fu, L.-L., 2008. The role of vorticity fluxes in the dynamics of the Zapiola Anticyclone. J. Geophys. Res. 113, C11015. http://dx.doi.org/10.1029/2008JC004841.
Weiss, J., 1991. The dynamics of enstrophy transfer in two-dimensional hydrodynamics. Physica D 48, 273–294.
Wunsch, C., Heimbach, P., Ponte, R., Fukumori, I., 2009. The global general circulation of the ocean estimated by the ECCO-consortium. Oceanography 22, 88–103.